RESEARCH AND APPLICATION OF MATERIALS SCIENCE

ISSN:2661-4464(online) 2661-4456(print)

Volume 4 No. 2 2022

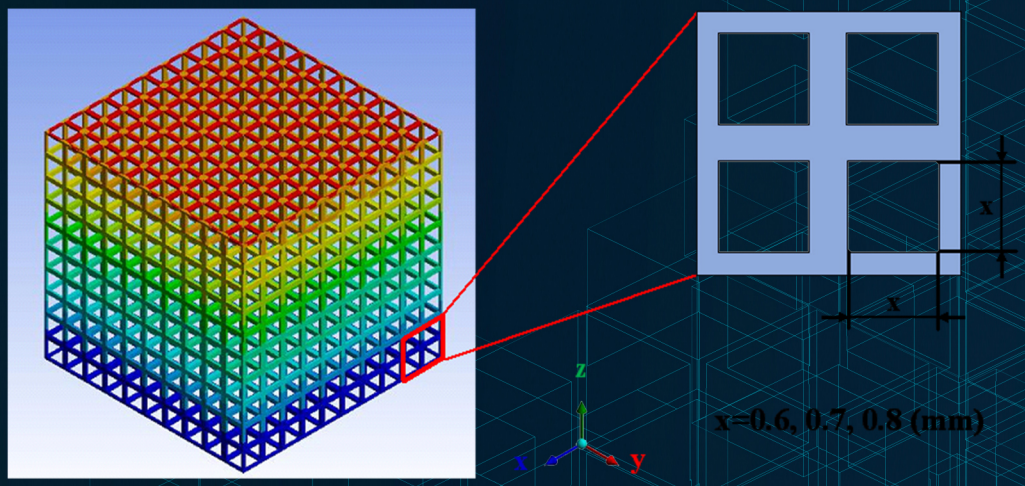

VISER

www.viserdata.com

COMPANY INTRODUCTION

Viser Technology Pte. Ltd. was founded in Singapore with branch offices in both Hebei and Chongqing, China. Viser focuses on publishing scientific and technological journals and books that promote the exchange of scientific and technological findings among the research community and around the globe. Despite being a young company, Viser is actively connecting with well-known universities, research institutes, and indexation database, and has already established a stable collaborative relationship with them. We also have a group of experienced editors and publishing experts who are dedicated to publishing high-quality journal and book contents. We offer the scholars various academic journals covering a variety of subjects and we are committed to reducing the hassles of scholarly publishing. To achieve this goal, we provide scholars with an all-in-one platform that offers solutions to every publishing process that a scholar needs to go through in order to show their latest finding to the world.

Research and Application of Materials Science

Publisher: Viser Technology Pte. Ltd.

ISSN: 2661-4464(online)

2661-4456(print)

Frequency: Semi-annual

Add.:21 Woodlands Close, #08-18

Primz Bizhub SINGAPORE (737854)

https://www.viserdata.com/

Research and Application of Materials Science

Volume 4 No.2 (2022)

CONTENTS

Message from "Special Issue of high entropy materials, powders, films, fibers and bulks"

In the past decades, the topic of high-entropy materials has made remarkable achievements and its application scope covers almost all kinds of fields. According the Shannon, entropy is the inverse of information, it indicates the randomness occupation of the components in the space, which is proportional to the content of the components if the system is completely random. Materials science is mainly focused on the topic of relation between the properties and micro- and nano- structures. In another word, the properties are determined by the micro- and nano- structures. Furthermore, the micro- and nano- structures can be adjusted by changing the compositions and processing. The high entropy conception extended the compositions of materials from the corner in the phase diagram to the center, and greatly increasing the composition space. Combining with the rapidly developed processing techniques, unique and wonderful structures in the micro- and nano- length scale of the high entropy materials are created and constructed, and the excellent properties are promising and expected. Research in the field of high-entropy materials is advancing rapidly. The special issue focuses on materials discovered using the high-entropy-alloy (HEA) and materials genome initiative (MGI) strategies. It discusses various types of high-entropy materials, such as face-centered cubic (FCC) and body-centered cubic (BCC) HEAs, films and coatings, wires and fibers, and powders and hard-cemented carbides.

In recent years, the high entropy materials is focusing on the studying of relationship among the properties, compositions, and processing; Summarizing industrially valuable alloys found in high-entropy materials that hold promise for promotion and applications; Explaining how high-entropy materials can be used in many fields and can outperform traditional materials.

In the future, high entropy materials with unique properties and excellent performance will be explored and used to replace tradition materials; new technologies, such as machine learning, data twinning, high throughput technology, will be used to design and develop the compositions and processing of the high entropy materials.

In order to timely reflect the latest research achievements of high entropy materials and provide opportunities for academic exchange, we specially organized a special issue of high entropy materials. Professor Yong Zhang of University of Science and Technology Beijing (USTB) was invited to organize this issue. Six articles will be published in this issue, the corresponding and/or first authors of the papers are Professor GH Geng, Professor G Li, Dr X Yang, Dr P Song, MS YQ Wu, and MS YX Wen, respectively, which ensured the publication of the special issue at a high level.

Finally, we would like to thank Professor Yong Zhang for his efforts in publishing this special issue. From the planning of the special issue, the organization of manuscripts, the recommendation of experts and the review of manuscripts, professor Zhang have given warm, rigorous and meticulous help in the whole process, which providing strong technical guarantee and selfless dedication for the academic quality of special issue. We also thanks MS QY Su, who devoted lots of efforts for this special issue. We would like to express our high respect and sincere thanks!

Planner Author

Yong Zhang graduated from Yanshan University with a bachelor's degree in 1991, and obtained a master's degree and PhD from the University of Science and Technology Beijing (USTB) in 1994 and 1998, respectively. Then he joined the Institute of Physics (IOP), Chinese Academy of Science (CAS), and worked as Postdoctoral Fellow. In 2000, he joined the Singapore-Massachusetts Institute of Technology (MIT) Alliance (SMA) and the National University of Singapore (NUS), and worked as Research Fellow in the program of Advanced Materials for Micro & Nano-Systems (AMM&NS). In 2004, he was promoted to Full Professor in 2004 at the USTB. In 2005, he was awarded the New Century Excellent Talent (NCET) by the Ministry of Education of China. He was a Senior Visiting Scholar at the University of Tennessee, Knoxville, USA.

He prepared the bionic dendrite and fish-bone structure of amorphous and highentropy composites by using the Bridgman-solidifi cation technique. He prepared the bionic bamboo-fi ber structure high-entropy wires by using cold-drawing methods. He prepared the glass-coated Cu alloy fi bers with shape-memory effect and super-elastic strain limits with bamboo-joint structures. He prepared the lotus-shaped amorphous porous alloys by using the etching technique. He prepared the fi rst single-crystal high-entropy alloys, Al 0.3 CoCrFeNi and Al 0.3 CoCrFeNi 2. The invention of trace rare earth elements can improve the glass-forming ability (GFA) of amorphous alloys, which has been widely used in academia and industries. The first body-centered cubic (BBC) alloy with high strength and high entropy was synthesized. The ratio parameter w of information entropy and mixing enthalpy was put forward to evaluate the disorder of materials, which has been proven by a large number of documents to be effective in predicting the formation of random solid-solution and amorphous phases.

High-entropy alloy fiber and high-entropy alloy photo-thermal selective films have been successfully studied. Professor Zhang participated in publishing the monograph Amorphous and High-Entropy Alloys; Advanced High-Entropy Alloys Technology ; High-Entropy Materials, A Brief Introduction; Magnetic Sensors-Development Trends and Applications ; Stainless Steels and Alloys ; Engineering Steels and HighEntropy Alloys ; High-Entropy Alloys, Fundamental and Applications ; High-Entropy

Alloys, Innovations, Advances, and Applications, and more. He participated in the Ministry of Education

Natural Science First Prize and Second Prize, the National Natural Science Second Prize, and the Shanxi Provincial Education Department Natural Science First Prize. He is also Member of the Amorphous Committee of the Metal Society, Fellow of the China Materials Research Society, and Fellow of the Nuclear Materials Society. Professor Zhang participated in organizing the conference on high-entropy alloys and serration behaviors, and served as Chair or Co-chair. He was Flexible Appointed Professor in the North Minzu University. He is also Science and Technology Correspondent of Guangdong Province and Guest Professor at North University of China. He has been selected as one of the thousand talents in Qinghai Province. He has edited the albums “Serration and Noise Behaviors in Advanced Materials”, “Nanostructured High-Entropy Alloys”, “The New Advances in High-Entropy Alloys”, and more. Professor Zhang devoted himself to studying serration behavior, high-throughput technology, and collective effect in materials science.

Professor Zhang has obtained 2 USA patents and 8 China patents, has published more than 200 papers, and has been cited more than 30,000 times. And one paper published in the journal Progress in Materials Science has been cited over 3,000 times. He is highly cited Author by Elsevier. He has published a paper in Science and reported in the paper Nature . He is Reviewer of many journal papers and books, including Nature, Science , Nature Reviews Materials , and Progress in Materials Science .

He is currently Editor-in-Chief of Journal of Metals, Section Editor-in-Chief of Journal of Metals and Entropic Alloys and Meta-Metals, and Associate Editor for Structural Materials in the Frontiers in Materials . He is also Editorial Committee Member of the journal Metals and Materials International. He is Editorial Board Member of the International Journal of Minerals, Metallurgy, and Materials (IJMMM), Metals World , Metals , and others; and Editorial Advisory Board Member of the journal of High Entropy Alloys and Materials .

Professor Zhang’s main research interest is the development of new materials in bulk, fi lm, and fiber forms by using high-entropy and Materials Genome Initiative (MGI) strategies to set up the relationship between micro- and nano-scale structures with their properties and performances.

About the Author

Ping Song, associate professor of Yanshan University. He received his doctor's degree from Beihang University in 2020. He hosted one National Natural Science Foundation project and one Hebei Natural Science Foundation project respectively. More than 25 SCI papers have been published in journals such as Solar Energy Materials and Solar Cells, ACS Applied Materials & Interfaces, Applied Physics Letters, and Physical Review Applied. Research interests include but are not limited to i) Preparation and multi-field regulation of antiferromagnetic materials, and related magnetic and electrical transport properties, such as pressure magnetic effect and anomalous Hall effect; ii) Preparation, structure and performance control of nano-magnetic functional materials; iii) Heat absorption, radiative cooling and other solar-thermal conversion devices, including solar spectrum selective absorption/radiation coating, high entropy materials, etc.

Guihong Geng is a professor in North Minzu University. He obtained his doctoral degree from the Chinese Academy of Space Technology in 2003. He has successfully completed one research project supported by the National Natural Science Foundation of China and is currently working on another. Additionally, he has led six research projects at the provincial and ministerial levels. Dr. Geng has published over 60 papers, including more than 30 papers indexed by SCI and EI. His primary research interests lie in the areas of metallic materials, materials processing engineering, and the utilization of composite field effects to address issues related to material segregation.

Xiao Yang is an associate researcher at Key Laboratory of Cryogenics, Technical Institute of Physics and Chemistry, Chinese Academy of Sciences. His research directions mainly focus on: the phase formation rule of high-entropy alloys (HEAs), synergistic mechanism of strengthening and corrosion resistance for high-performance HEAs, and the high-gravity (extreme) preparation technology of HEAs. The representative scientific research achievements are as follows: (1) A new criterion for the formation of multi-component solid solutions in HEAs was proposed, namely: $\Omega \geqslant 1.1$ and $\delta \leqslant 6.6$ %. This phase formation criterion has been used as a semi-empirical criterion for the composition design of HEAs, and has been widely used by domestic and foreign counterparts. The work was published in Materials Chemistry and Physics. (2) The entropy stability design theory of precipitation-strengthened FCC structure HEAs was proposed, and a HEA system with high strength, high toughness and high corrosion resistance was developed. The comprehensive properties of this alloy have reached the international advanced level. (3) A high-gravity combustion synthesis special preparation technology suitable for the preparation of high-entropy alloys has been developed, which realizes the low-cost and efficient preparation of high-entropy materials, and provides a new way for the large-scale production and application of high-entropy materials. Based on the above achievements, he has published more than 40 academic papers with a total of over 3,000 citations, and has applied for 9 national invention patents, 6 of which have been authorized, and has published one book of Advanced Technology in High-entropy Alloys.

About the Author

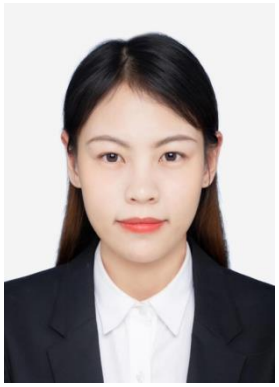

Yuxin Wen is a Master degree candidate at the University of Science and Technology Beijing (USTB), supervised by Prof. Zhang Yong. Her research work focuses on "copper-based high-entropy alloys with high strength and high conductivity". She studied The effect of binder phase content on WC-AlCoCrFeNiTi0.2 high entropy cemented carbides microstructure and mechanical properties, which have been published in 《Materials Reports》. In addition, she had co-edited an English book chapters with Professor Zhang. The title of the book is “High-entropy materials: advances and applications”, by CRC press, the chapter title is: “High-Entropy Powder and Hard-Cemented Carbide Alloys”.

Gong LI received her PhD in Condensed mater physics, Institute of Physics, Chinese Academy of Sciences. After post-doctoral position in Metal physics at Max-Planck-Institut für Metal, financial supported by Max-Planck Society, she got a professor position at State Key Laboratory of Metastable Materials Science and Technology, Yanshan University. From Feb 2012-Feb 2017, she got her visiting position in The University of Tennessee, and doing research on disordered multi-principal element alloys using synchrotron in APS, Argonne, and neutron in ORNL, Oak ridge. Then on Mar-June 2019 in Rice University, Texas, she did scientific research on Bio-materials. Her current research interests are phase transitions driven properties optimization under extreme condition in disordered system, including metal, inorganic non-metal and small organic materials by synchrotron/neutron resources.

Yaqi Wu is a PHD candidate at the University of Science and Technology Beijing (USTB), supervised by Prof. Zhang Yong. Her research work is focused on the topic of “amorphous alloys” and “designing and component optimizing of soft magnetic high-entropy alloys by using materials genome initiative (MGI)”. She proposed “Three-dimensional balanced growth theory” for the amorphous alloys and published a review article on the journal of Frontiers material. In 2021, she prepared the body centered cubic (BCC) structured TiZrNbMoV high-entropy alloy by using powder sintering, studied the mechanical behaviors, and the related results had been published on the journal of Metals. In the same year, she applied a patent for high throughput screening of high entropy alloys and obtained a licensed software copyright of the phase formation rule calculation. In addition, she had co-edited two English book chapters with Professor Zhang. The title of the first book is “Advances in High-Entropy Alloys: Materials Research, Exotic Properties and Applications”, by Intechopen publisher, the chapter title is: “Desigh and High-Throughput Screening of High-etropy Alloys”; the title of the second book is: “High-entropy materials: advances and applictions”, by CRC press, the chapter title is: “High-Entropy Ceramics and Intermetallic Compounds”.

Viser Technology Pte. Ltd.
Research and Application of Materials Science
DOI: 10.33142/rams.v4i2.8463

Research Article Open Access

Enhancement of Near-Field Radiative Heat Transfer based on High-Entropy Alloys

Shanshan DENG, Ping SONG*, Boxi ZHANG, Sen YAO, Zhixin JIN, Defeng GUO

State Key Laboratory of Metastable Materials Science and Technology and Key Laboratory for Microstructural Material Physics of Hebei Province, School of Science, Yanshan University, Qinhuangdao 066004, P. R. China

***Corresponding Author:** Ping Song,e-mail: psong@ysu.edu.cn*

Abstract:
The enhancement of near-field radiative heat transfer (NFRHT) has now become one of the research hotspots in the fields of thermal management and imaging due to its ability to improve the performance of near-field thermoelectric devices and near-field imaging systems. In this paper, we design three structures (multilayer structure, nanoporous structure, and nanorod structure) based on high-entropy alloys to realize the enhancement of NFRHT. By combining stochastic electrodynamics and Maxwell-Garnett's description of the effective medium, we calculate the radiative heat transfer under different parameters and find that the nanoporous structure has the largest enhancement effect on NFRHT. The near-field heat transfer factor (q) of this structure ($q = 1.40\times10^{9}$ W/ (m^2 K)) is three times higher than that of the plane structure ($q = 4.6\times10^{8}$ W/ (m^2 K)), and about two orders of magnitude higher than that of the SiO_2 plate. This result provides a fresh idea for the enhancement of NFRHT and will promote the application of high-entropy alloy materials in near-field heat radiation.

Keywords: *near-field radiative heat transfer; high-entropy alloys; multilayer structure; nanoporous structure; nanorod structure*

1 Introduction

Near-field radiative heat transfer (NFRHT) has become a hot topic in the fields of thermoptoelectronics [1-5], energy harvesting [6-8], sensing [9-10], and thermal management [11-13]. When the distance between two objects is at the nanometer level, the NFRHT can break the limit of Planck's law due to the coupling of photon tunneling and evanescent waves. This may be several orders of magnitude larger than the far-field heat transfer between two black bodies. To date, NFRHT has been studied in some isotropic and anisotropic materials. For isotropic materials, e. g., graphene, doped silicon, and gold, structures such as nanowires, nanopores, multilayer membranes, and 1D gratings have been designed to obtain a higher heat flow [14-21]. Graphene plasmons can couple evanescent waves in a near-field resonance, thereby enhancing the radiative heat flux through the nanoscale vacuum gap. Van Zwol et al. [14] demonstrated that the NFRHT between SiO_2 microspheres and the substrate was significantly increased by a single layer or several layers of graphene lying on the SiC substrate. Liu et al. [16] found that both doped silicon nanowires and nanopores can achieve an order of magnitude enhancement than bulk-doped silicon. Guerot et al. [21] predicted that the heat transfer between two gold gratings was increased by an order of magnitude more than that between two gold substrates. For anisotropic materials, the natural hyperbolic hexagonal boron nitride (hBN) has been mainly studied [22-24], which can support multiple orders of phonon-polaritonic waveguide modes in its two infrared bands. Surface plasmons in graphene can couple with the phonon polaritons in hBN films to form hybrid polaritons that greatly enhance photon tunneling and then enhance the NFRHT. Zhao et al. [22] found that monolayer graphene on hBN films is more than twice as heterogeneous as graphene monolayer or hBN films. Shi et al. [24] demonstrated that a multilayered structure consisting of five or more graphene-hBN units has a thermal flux four orders of magnitude larger than the black body.

Recently, we have studied the thermal radiation based on high-entropy alloys and found a broadband and wide-temperature-range thermal emission effect of high-entropy alloys [25]. This result predicts the possibility of applying high-entropy alloys to the field of NFRHT. In this paper, we combine hyperbolic materials hBN and high-entropy alloys to form multilayer metasurface structure and use high-entropy alloys to form nanoporous and nanorod structures. By changing the different parameters of the structure and materials, the optimal structure that maximizes the NFRHT efficiency is obtained. It is found that the nanoporous structure has the largest enhancement effect on NFRHT. The near-field heat transfer ability of this structure is two

Received on November 1, 2022; Accepted on December 11, 2022

orders of magnitude higher than the heat transfer rate of the SiO_2 plate under the same conditions.

2 Experiment

NiCrCuFeSi (referred to as NCCFS) high-entropy alloy is selected as the object to study NFRHT. To make the high-entropy alloy have better and more meaningful characteristics, we choose to use the nitrided NCCFS alloy (referred to as (NCCFS) N) for research and analysis [26]. The nitrogen content is determined by the nitrogen flow rate x.

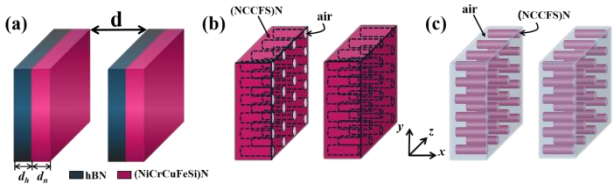

Figure 1 Schematic diagram of three structures based on the high-entropy alloys. (a) Multilayer structure. (b) Nanoporous structure. (c) Nanorod structure

We simulated the heat transfer factor under the optimal structure to explore the actual enhancement of NFRHT between parallel structures. Our first structure uses (NCCFS)N and hyperbolic hexagonal boron nitride (hBN) as materials to design a multilayer structure, as shown in Figure 1(a). Two flat plates are semi-infinite media, and d is the distance between two parallel plates. The thickness of the metal layer (NCCFS) N is expressed as d_n, and the thickness of the medium layer hBN is expressed as d_h. The dielectric function has a general expression in theory [27]:

$$\varepsilon(\omega)=1+\sum_j \frac{\omega_{p,j}^2}{\omega_{g,j}^2-\omega^2-2i\omega\gamma_j} \tag{1}$$

where ω is the frequency of the incident electromagnetic wave, $\omega_{p,j}$ the plasma frequency, $\omega_{g,j}$ the response frequency, γ_j the damping coefficient. The dielectric function model in this study is mainly the Drude model [28] applicable to metal materials. Its motion equation is:

$$m\ddot{x}+m\gamma\dot{x}=-eE_0\exp(-i\omega t) \tag{2}$$

where m is the electron mass and e is the charge and electric quantity. The real part (ε_1) and the imaginary part (ε_2) of the dielectric function can be deduced from the equation [16]. The expressions are:

$$\varepsilon_1(\omega)=1-\frac{\omega_p^2}{\omega^2+\gamma^2} \tag{3a}$$

$$\varepsilon_2(\omega)=1-\frac{\omega_p^2}{\omega^3+\gamma^2\omega} \tag{3b}$$

$$\omega_p^2=\frac{Ne^2}{m\varepsilon_0} \tag{3c}$$

In this paper, the real part and imaginary part of the dielectric function of (NCCFS) N high-entropy alloy at different nitrogen concentrations are from Ref. [26]. For multilayer parallel structures formed by alternate combination, $\varepsilon_x=\varepsilon_y=\varepsilon^{\parallel}$, $\varepsilon_z=\varepsilon^{\perp}$, its dielectric function formula is as follows [29]:

$$\varepsilon^{\perp}=\frac{\varepsilon_n d_n+\varepsilon_h d_h}{d_n d_h} \tag{4a}$$

$$\varepsilon^{\parallel}=\frac{d_n+d_h}{d_n/\varepsilon_n+d_h/\varepsilon_h} \tag{4b}$$

Our other two structures are the alternative combination of high-entropy alloy and air to form nanoporous or nanorod structures, as shown in Figure 1(b) and 1(c). In Maxwell – Garnett theory, the effective properties of composite media are obtained by taking one component of the composite as the substrate and embedding all other components into the substrate as filler materials. The materials do not contact each other. The relationship between dielectric functions in different directions and material parameters under nanoporous structure is as follows:

$$\frac{\varepsilon^{\parallel}-\varepsilon_a}{\varepsilon^{\parallel}+\varepsilon_a}=f\frac{\varepsilon_n-\varepsilon_a}{\varepsilon_n+\varepsilon_a} \tag{5a}$$

$$\varepsilon^{\perp}-\varepsilon_a=f(\varepsilon_n-\varepsilon_a) \tag{5b}$$

$$f_1=\frac{Vair}{V_{(NCCFS)N}} \tag{5c}$$

From the above formula, it can be deduced that the dielectric function expressions of the electric field parallel to the optical axis and perpendicular to the optical axis in the nanoporous structure are respectively:

$$\varepsilon^{\parallel}=\frac{2\varepsilon_a}{1-f_1\frac{\varepsilon_n-\varepsilon_a}{\varepsilon_n+\varepsilon_a}}-\varepsilon_a \tag{6a}$$

$$\varepsilon^{\perp}=f_1(\varepsilon_n-\varepsilon_a)+\varepsilon_a \tag{6b}$$

where f_1 refers to the volume filling rate of the nanoporous structure, which is equivalent to a controllable constant in the program, ε_n the dielectric function of the high entropy alloy, ε_a the dielectric constant of air, ε_z the dielectric function of the electric field along the optical axis. Because it is equivalent to the weighted average of the dielectric functions of (NCCFS) N film and air, it is essentially determined by a weakened Drude model.

For the nanorod structure, it is equivalent to the opposite of the nanoporous structure, that is, the columnar filling of the high-entropy alloy is carried out with air as the substrate. The dielectric function formula of nanorod structure is ε_n and ε_a after the position is changed, the filling ratio f_1 is the reciprocal of f_1. Biehs et al. calculated the heat transfer factor (q) between two anisotropic planar media separated by the true space gap d at the temperature T [30].

$$q=\frac{1}{8\pi^3}\int_0^{\infty}g(\omega,T)d\omega\int_0^{2\pi}\int_0^{\infty}\xi(\omega,\beta,\phi)\beta d\beta d\phi \tag{7a}$$

$$g(\omega,T)=\frac{\partial}{\partial T}\left(\frac{\hbar\omega}{e^{\hbar\omega/k_BT}-1}\right)=\frac{(\hbar\omega)^2e^{\hbar\omega/k_BT}}{k_BT^2(e^{\hbar\omega/k_BT}-1)^2} \tag{7b}$$

where the $\xi(\omega,\beta,\varphi)$ is the energy transmission coefficient. The heat transfer factor can directly reflect the efficiency of heat transfer. This paper discusses the enhancement of NFRHT by calculating the heat transfer factor.

3 Results and discussion

A. Enhancement of NFRHT by multilayer structure

The simulated result of the multilayer structure is shown in Figure 2(a). The value of q can be tuned by the distance between parallel plates (d) and the thickness ratio between (NCCFS)N film and Hbn (d_n/d_h). As shown in Figure 2(a), the value of q increases with the decrease of d and will have a sharp increase when d $<$ 30 nm. When changing the d_n/d_h, the value of q no longer varies monotonically as d_n/d_h changes. It's going to peak at a certain value of d_n/d_h. The maximum value of q is 3.84×10^8 W/ (m^2 K) at d_n/d_h = 0.1 when d = 30 nm. This result is 17.8% higher than that of a single Hbn film (q = 3.26×10^8 W/ (m^2 K)). We further investigate the nitrogen content (x) effect on q. As shown in Figure 2(b), with the increase of x, the value of q shows a trend of increasing first and then decreasing. When x = 1.0 sccm, the value of q reaches a peak of 4.64×10^8 W/ (m^2 K), which is 1.4 times higher than that of a single Hbn film.

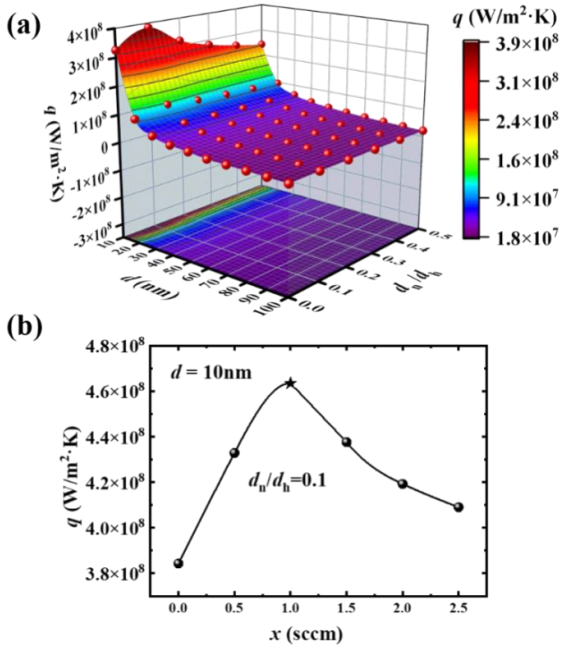

Figure 2 (a) q value of multilayer structure under different conditions. (b) The effect of nitrogen flow x on q under the condition of d = 10 nm and d_n/d_h = 0.1

B.Enhancement of NFRHT by nanoporous structure

To further increase the near-field heat transfer performance of high-entropy alloys, we designed the metastructure of the nanoporous structure. As shown in the inset of Figure 3, nanoporous (NCCFS)N materials are designed and the dimension scale of the nanoporous structure is defined by the volume filling ratio of air ($f_1 = V_{air}/V_{(NCCFS)N}$). The simulated values of q under different f_1 are shown in Figure3. When the distance (d) between the two nanoporous structures (as shown in Figure 1(b)) is fixed, the value of q increases gradually with the increase of f_1 and it reached 1.40×10^9 W/(m^2 K) at f_1 = 0.9. This result is about 20 times that of f_1 = 0 and is 2 orders of magnitude higher than the heat transfer rate of the SiO_2 plate under the same conditions. This may be due to the additional surface waves in the nanoporous structure generating supplementary heat transfer channels in the entire gap.

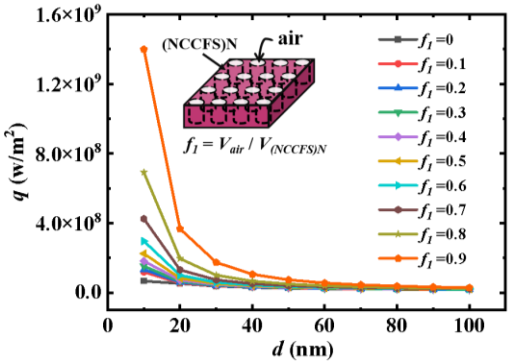

Figure 3 Distance between the two nanoporous structures (d) dependence of q under different f_1

C.Enhancement of NFRHT by nanorod structure

We also design the nanorod structure based on the (NCCFS)N high-entropy alloys and the dimension scale of the nanorod structure is defined by the volume filling ratio of the (NCCFS)N high-entropy alloys (as shown in the inset of Figure4). The simulated values of q under different f_2 are shown in Figure4. At the certain d value, the heat transfer factor of the nanorod structure decreases with the increase of f_2. The maximum value of q is 7.70×10^8W/ (m^2 K) at f_2 = 0.1 and d= 10 nm and this value of q is about 11 times that of f_2 = 1.

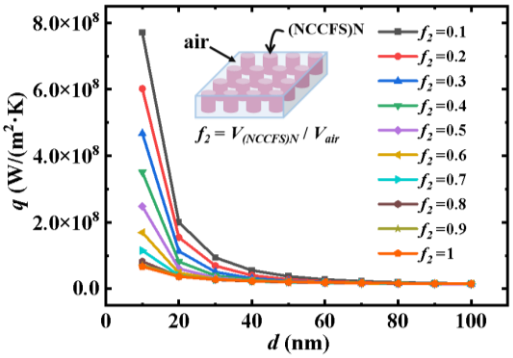

Figure 4 Distance between the two nanorod structures (d) dependence of q under different f_2

4 Conclusion

In summary, we calculated the heat transfer factors of multilayer structure, nanoporous, and nanorod structures designed based on (NCCFS) N high-entropy alloys under different parameters. The simulation results show that these three types of structures can effectively enhance near-field heat radiation. From the comparison of three structures and different material parameters, the nanoporous structure is the optimal structure for near-field heat transfer enhancement. The maximum q value is taken when d = 10 nm, f_1 = 0.9, and q = 1.40×10^9W/ (m^2 K), which is about 20 times that of f_1 = 0 and is 2 orders of magnitude higher than the heat transfer rate of the SiO_2 plate under the same conditions.

This may be due to the existence of additional surface waves in the nanoporous structure, which generates supplementary heat transfer channels in the entire gap. Our result will promote the application of high-entropy alloys in energy collection and thermal management.

Acknowledgments

This work is supported by the National Natural Science Foundation of China (Grant Nos. 52101233, 51931007, and 52071279), the Hebei Natural Science Foundation (No. E2022203010), and the Innovation Capability Improvement Project of Hebei Province (No. 22567605H).

References

[1] A. Karalis, J.D. Joannopoulos. Transparent and 'opaque' conducting electrodes for ultra-thin highly-efficient near-field thermophotovoltaic cells ,Sci Rep [J]. 7(2017): 14046.

[2] A. Fiorino, L. Zhu, D. Thompson, et al.. Nanogap near-field thermophotovoltaics, Nat Nanotech [J]. 13(2018): 806-811.

[3] R. Vaillon, J.P. Pérez, C. Lucchesi, et al.. Micron-sized liquid nitrogen-cooled indium antimonide photovoltaic cell for near-field thermophotovoltaics, Opt. Express [J]. 27 (2019) A11.

[4] G.T. Papadakis, S. Buddhiraju, Z. Zhao, et al.. Broadening Near-field emission for performance enhancement in thermophotovoltaics, Nano Lett [J]. 20 (2020) 1654-1661.

[5] B. Zhao, K. Chen, S. Buddhiraju, et al.. High-performance near-field thermophotovoltaics for waste heat recovery, Nano Energy. 41 (2017):344-350.

[6] J.Y. Chang, Y. Yang, L. Wang. Tungsten nanowire based hyperbolic metamaterial emitters for near-field thermophotovoltaic applications, Int. J. Heat Mass Transfer [J]. 87 (2015):237-247.

[7] S.A. Biehs, M. Tschikin, R. Messina, et al.. Super-Planckian near-field thermal emission with phonon-polaritonic hyperbolic metamaterials, Appl Phys. Lett [J]. 102 (2013):131106.

[8] M.S. Mirmoosa, F. Rüting, I.S. Nefedov, et al.. Effective-medium model of wire metamaterials in the problems of radiative heat transfer, J. Appl. Phys [J]. 115 (2014) 234905.

[9] R. Schilling, H. Schütz, A.H. Ghadimi, et al.. Near-field integration of a SiN nanobeam and a SiO_2 microcavity for heisenberg-limited displacement sensing, Phys. Rev. Applied [J]. 5 (2016) 054019.

[10] R.I. Stantchev, D.B. Phillips, P. Hobson, et al.. Compressed sensing with near-field THz radiation , Optica [J]. 4 (2017) 989.

[11] Y. Yang, S. Basu, L. Wang, Radiation-based near-field thermal rectification with phase transition materials, Appl. Phys. Lett [J]. 103 (2013) 163101.

[12] Y. Yang, S. Basu, L. Wang, Vacuum thermal switch made of phase transition materials considering thin film and substrate effects, J. Quant. Spectrosc. Ra [J]. 158 (2015) 69-77.

[13] P. Ben-Abdallah, S.A. Biehs, Phase-change radiative thermal diode, Appl. Phys. Lett [J]. 103 (2013) 191907.

[14] P.J. van Zwol, S. Thiele, C. Berger, et al.. Nanoscale radiative heat flow due to surface plasmons in graphene and doped silicon, Phys. Rev. Lett [J]. 109 (2012) 264301.

[15] A.I. Volokitin, B.N.J. Persson, Near-field radiative heat transfer between closely spaced graphene and amorphous SiO_2, Phys. Rev. B [J]. 83 (2011) 241407.

[16] X.L. Liu, R.Z. Zhang, Z.M. Zhang, Near-field radiative heat transfer with doped-silicon nanostructured metamaterials, Int. J. Hate Mass Tran [J]. 73 (2014) 389–398.

[17] S. Basu, L. Wang, Near-field radiative heat transfer between doped silicon nanowire arrays, Appl. Phys. Lett [J]. 102 (2013) 053101.

[18] P. Song, Y. Wu, L. Wang, et al.. The investigation of thermal stability of Al/NbMoN/NbMoON/SiO_2 solar selective absorbing coating, Sol. Energy Mater Sol. Cells [J]. 171 (2017) 253–257.

[19] C.J. Fu, Z.M. Zhang, Nanoscale radiation heat transfer for silicon at different doping levels, Int. J. Heat Mass Tran [J]. 49 (2006) 1703–1718.

[20] A. Kittel, W. Müller-Hirsch, J. Parisi, S.A. Biehs, et al.. Near-field heat transfer in a scanning thermal microscope, Phys [J]. Rev. Lett. 95 (2005) 224301.

[21] R. Guérout, J. Lussange, F.S.S. Rosa, et al.. Enhanced radiative heat transfer between nanostructured gold plates, Phys Rev. B [J]. 85 (2012) 180301.

[22] B. Zhao, Z.M. Zhang, Enhanced photon tunneling by surface plasmon–phonon polaritons in graphene/hBN heterostructures, J. Heat Transfer [J]. 139 (2017) 022701.

[23] B. Zhao, B. Guizal, Z.M. Zhang, et al.. Near-field heat transfer between graphene/hBN multilayers, Phys Rev. B [J]. 95 (2017) 245437.

[24] K. Shi, F. Bao, S. He, Enhanced near-field thermal radiation based on multilayer graphene-hBN heterostructures, ACS Photonics [J]. 4 (2017) 971–978.

[25] P. Song, C. Wang, Y. Sun, et al.. Broadband and wide-temperature-range thermal emitter with super-hydrophobicity based on oxidized high-entropy film, ACS Appl Mater [J]. 12 (2020) 4123–4128.

[26] P. Song, C. Wang, J. Ren , et al.. Modulation of the cutoff wavelength in the spectra for solar selective absorbing coating based on high-entropy films., Int. J. Mine. Metall Mater [J]. 27 (2020) 1371–1378.

[27] M. Cardona, Modulation Spectroscopy, Academic Press, New York [D], 1969.

[28] P. Drude, The Theory of Optics, Dover Publications, New York [D], 1925.

[29] S. Basu, B.J. Lee, Z.M. Zhang, Near-field radiation calculated with an improved dielectric function model for doped silicon, J. Heat Transfer [J]. 132 (2010) 023302.

[30] K. Joulain, J.P. Mulet, F. Marquier, et al.. Surface electromagnetic waves thermally excited: Radiative heat transfer, coherence properties and Casimir forces revisited in the near field, Surf. Sci. Rep [J]. 57 (2005) 59–112.

Viser Technology Pte. Ltd.
Research and Application of Materials Science
DOI: 10.33142/rams.v4i2.8464

Research Article Open Access

Structure evolution in undercooled CoCrNi medium entropy alloys by glass fluxing method

Subo YU, Aleksandr SHERSTNEV, Mikhail MARKOVSKII, Daria KATAITSEVA, Gong LI *

State Key Laboratory of Metastable Materials Science and Technology, Yanshan University, Qinhuangdao 066004, People's Republic of China

***Corresponding Author:** *Gong LI: gongli@ysu.edu.cn*

Abstract:
Undercooling of ternary CoCrNi medium entropy alloy (MEA) was achieved by molten glass fluxing method. The influence of undercooling on microstructure and mechanical properties of was investigated. The microstructure changes during the undercooling process identified by transmission electron microscope and scanning electron microscope shows that the grain size and intergranular phase all change after the undercooling treatment. The yield strength of the ternary MEA increased significantly after undercooling treatment, which attribute to the refined grain size and the formation of the new phase. Undercooling method can be used as a potential method to modify the microstructure and improve the mechanical properties of MEAs.
Keywords: *Medium-entropy alloy; undercooling; microstructure; mechanical properties*

1 Introduction

Traditional alloys include one or two principal elements, but high entropy alloys (HEAs) have broken the traditional concept defined by Yeh et al. [1-4], which brings many challenges and opportunities for the traditional material industry. Different from traditional alloys, although HEAs are composed of multiple elements, these alloys tend to form simple structures rather than complex intermetallic compound such as face-centered-cubic (FCC), body-centered-cubic (BCC), hexagonal-close-packed (HCP) or a mixture of FCC and BCC [3]. Since the mixing entropy of the HEA is very high, when the component increases, the high entropy effect enhances the mutual solubility of alloying elements, which inhibits the formation of intermetallic compounds and complex phases, and promotes the appearance of simple solid solutions [5-7]. Compared with conventional alloys, HEAs have lots of outstanding properties such as high hardness, good high temperature strength, potential to be thermoelectric materials, great resistance to friction, oxidation, corrosion, evaluation wear and fatigue [3, 8-19]. Recently, equiatomic ternary and quaternary high-entropy alloys have also attracted the attention of researchers with the development of the research on high-entropy alloys [21-22] for being model alloys because of the less elements.

Rapid solidification is one of the most active fields in metal materials research and have attracted great interest in recent years [22-24]. Compared with conventional solidification, rapid solidification is a typical non-equilibrium process, and its main characteristics are as follows: with the increasing of the solidification rates, the distribution of solutes will deviate from equilibrium and the microstructure of the alloy will be greatly refined. Under the condition of rapid solidification, the precipitation of the equilibrium phase is inhibited and the metastable phase is precipitated. In the rapid solidification processes, the cooling rate can reach 10^5 K/s [25], such a high cooling rate can lead to considerable undercooling. Undercooling technique [26-27] enables a bulk alloy rapidly solidification. In 1951, Turnbull achieved an undercooling of 80 K in mercury [28]. There are several ways to achieve undercooling, including glass fluxing method [29], electromagnetic levitation [30] and drop tube technique [31-32]. Li et al. research on CoCrFeNi high entropy alloy has been solidified with a high undercooling up to 300 K adopting glass fluxing method. It is known that CoCrFeNi HEA possesses a single-phase FCC structure. Different from the as-cast sample with solely FCC structure, the sample solidified with a large undercooling of 300 K shows a mixture of FCC and BCC phase [33]. The undercooling method is an effective way to obtain metastable phase and refine grain structure in the solidification treatment [34-35]. The purpose of this paper is to invest the evolution of the microstructure and mechanical properties of CoCrNi ternary medium entropy alloy (MEA) after glass fluxing treatment.

2 Experimental

The alloy was prepared by the arc-melting method in a vacuum-titanium-gettered high purity argon (99.999

Received on November 10, 2022; Accepted on December 15, 2022

volume percent, vol %) which using high purity (99.95 wt %) raw elements of cobalt, chromium, and nickel and cooled by the water in a copper crucible. To ensure the homogeneity of the sample, these materials were flipped and remelted at least five times. The glass fluxing method was used in the undercooling experiment. The high-entropy alloy was melted in the high-frequency furnace under an argon gas together with B_2O_3 glass. It is generally believed that the purification process of molten glass plays a role in two aspects, on the one hand, the molten glass covers the surface of the metal melt to isolate air and liquid metal, and inhibits the nucleation caused by oxides. On the other hand, the melt is separated from metal oxides and impurities by the viscous adsorption and chemical reaction of the molten glass to achieve physical or chemical purification. It has been proved that the molten B_2O_3 glass does not react with the sample. Before the experiment, the B_2O_3 was dehydrated in the muffle furnace at 873 K for 2 h. The alloy and the B_2O_3 glass were put in the quartz tube and adjust the relative position between the alloy and the induction coil so that the sample is in the middle of the coil. When heated, the B_2O_3 glass will melt and wrap the metal sample in it. In this way, it can effectively prevent the metal from oxidizing during the melting process and contact with the wall. In addition, deep undercooling can achieve the ideal degree of undercooling, so as to realize rapid solidification of metal at relatively slow cooling rate. In our study, natural cooling can be used for rapid solidification process without fast cooling rate [36-37].

Crystal structure was identified by X-ray diffraction (XRD), which is a D/MAX-2500/PC X-ray diffractometer instrument equipped with Cu-Kα radiation (λ= 1.54056 Å), and scanning was performed over the range of two theta (2θ) from 20° to 100° with a speed of 4 °/min. Microstructure was characterized by optical microscope (Axiovert 200MAT), scanning electron microscopy (SEM, Hitachi S-4800 microscope). The device is equipped with energy-dispersing X-rays Diffraction spectra (EDS). The components of precipitated phase in CoCrNi alloy were analyzed by EDS patterns. Before SEM observation, proceed first cutting, mosaic, mechanical grinding, polishing, cleaning, blow drying, corrosion, cleaning, blow drying and other steps to prepare the sample.

Transmission electron microscopy (TEM) were conducted on a Talos F200X instrument facility operating at 200 kV. The microstructure of the samples was also characterized by TEM. The TEM image of the sample and the corresponding selected area electron diffraction (SAED) of the image are obtained. TEM slices were mechanically grounded to 50 μm, and then twin-jet polished in a solution of 10 vol % perchloric acid and 90 vol % carbinol at 20 V.

A universal compression machine (INSTRON-5982) was employed at room temperature with an engineering strain of 5×10^{-4} s^{-1}. The cylindrical samples for compression have a size of Φ 3×6 mm. More than 3 times measurements were repeated for each alloy to obtain the accurate data. The Vickers hardness was determined on HVS-1000 under a load of 500 g for 10 s. The mean value from ten measurements was taken for each sample.

3 Results and discussion

3.1 Microstructure Characterization

Figure 1 presents the XRD patterns of CoCrNi MEA solidified at as-cast and undercooled conditions. The as-cast CoCrNi MEA alloy has a typical single-phase FCC structure, and after the undercooling treatment, new phases are precipitated, but the FCC phase is still the main phase of the sample. The diffraction peak of the precipitated new phase coincides with the CoCr hexagonal-close-packed phase (HCP) diffraction peak. The XRD results show that the undercooling treatment can lead to the change of the internal structure of the ternary high-entropy alloy [38].

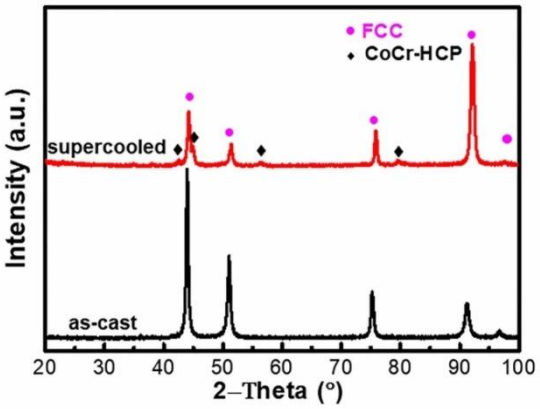

Figure 1 XRD patterns of CoCrNi MEA at as-cast and undercooled conditions

Identifying the microstructure changes of the CoCrNi MEA during the undercooling process by SEM and TEM is crucial for elucidating the machinal propertied promotion after the undercooling treatment. Figure 2(a) shows SEM images of the as-cast CoCrNi MEA. The solidified structure of CoCrNi MEA after undercooling treatment were shown in Figure 2(b). The as-cast CoCrNi alloy has a single-phase FCC structure with a large grain size of approximately 500 μm. After the undercooling treatment, the grain size of the sample significantly refined [35, 38-39]. A dendrite structure of the precipitated phase can be found in CoCrNi alloy. The precipitated phase is a Co-, Cr-rich phase which was identified by EDS patterns shown in Figure 2(c).

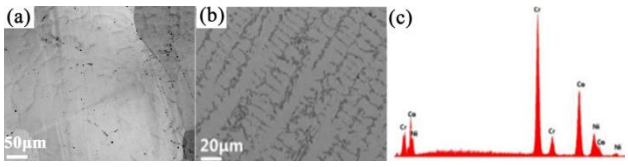

Figure 2 (a) SEM images of the as-cast CoCrNi MEA(b) SEM images of CoCrNi MEA after undercooling treatment, (c) EDS of precipitation phase in the CoCrNi MEA

In order to further reveal the effect of undercooling on the medium entropy alloys, TEM analyze were carried out. Figure 3 is the TEM images of CoCrNi MEA, Figure 3(a) is the microstructure of the matrix. We can see that there is nanophase precipitation on the FCC matrix. The darker areas are precipitated phases, and the size of the precipitated phase is about 20 nm. The spots with higher brightness shown in Figure 3(b) are SAED patterns of FCC matrix phase. Due to the thickness of the sample or the high energy of the incident electron, secondary diffraction is caused, resulting in the formation of secondary diffraction spots. Figure 3(c) is the microstructure of the interdendrite phase, and Figure 3(d) is the diffraction spots. Combined with the diffraction spots, we can see that the interdendrite phase is hexagonal phase. The stacking fault energy of CoCrNi is relatively low. Due to rapid solidification after deep undercooling, the HCP phase was precipitated by martensitic transformation at FCC. This is like the quenching of martensite in steel [40-41].

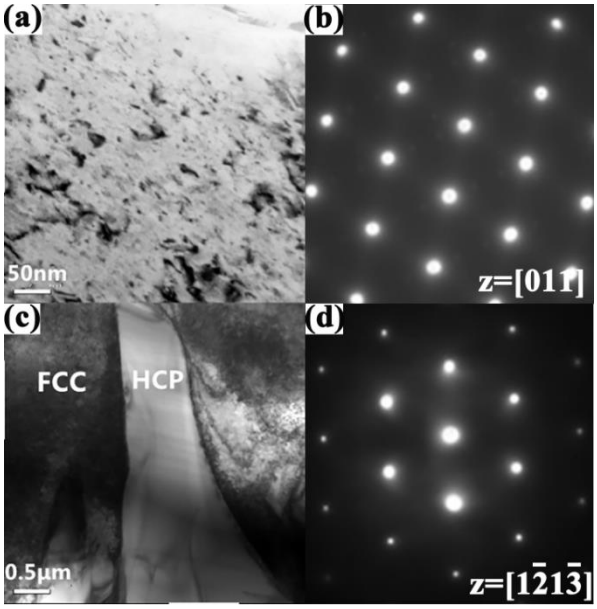

Figure 3 (a) TEM images of CoCrNi matrix, (b) SAED patterns of matrix, (c) TEM images of CoCrNi precipitation phase, (d) SAED patterns of precipitation phase

In the undercooling melt, there is a great driving force for crystal growth [31-35]. If nucleation occurs, the crystal will start to grow at a very fast rate, and then a large amount of crystal will be quickly released during the rapid growth of the crystal. The latent heat of crystallization leads to the re-glow phenomenon, which causes the temperature to rise rapidly until it is near the liquidus line, therefore the newly formed dendrites are under severe overheating, which leads to the occurrence of remelting [34-35]. The remelting of dendrites will lead to the apparent refinement of grains.

3.2 Mechanical Properties

The mechanical properties of the CoCrNi MEA were investigated and shown in Figure 4. From the strain-stress curves (Figure 4a) and hardness of CoCrNi MEA (Figure4 b), we can see that the plasticity and Vickers hardness of the ternary alloys after undercooling have been significantly improved. It shows that the room temperature compressibility of CoCrNi alloy has been greatly improved, and the yield strength has been increased from 180 MPa to 900 MPa. Hardness is a measure of the ability of the object to resist deformation, and it is a means of characterizing the mechanical properties of the material. The Vickers hardness of the CoCrNi alloy has been increased from 183 HV to 328 HV. The reason of the room temperature compression performance and Vickers hardness improved after undercooling treatment is that the grain size of the sample is significantly refined and the precipitation of the hard and brittle phase [35, 38]. The phase interface of FCC and HCP will hinder the dislocation movement, and dislocation plug will be formed at the phase boundary. Due to the toughness of FCC, the stress concentration caused by dislocation plugging can be relieved by the deformation of FCC in the deformation process to a certain extent, and the stress of micro-crack formation can be increased, thus improving the tensile strength and hardness [42-43]. The precipitation of the nano-precipitated phase in the matrix plays a key role in precipitation strengthening, resulting in a significant increase in the strength of the alloy and compressibility at room temperature [44-46].

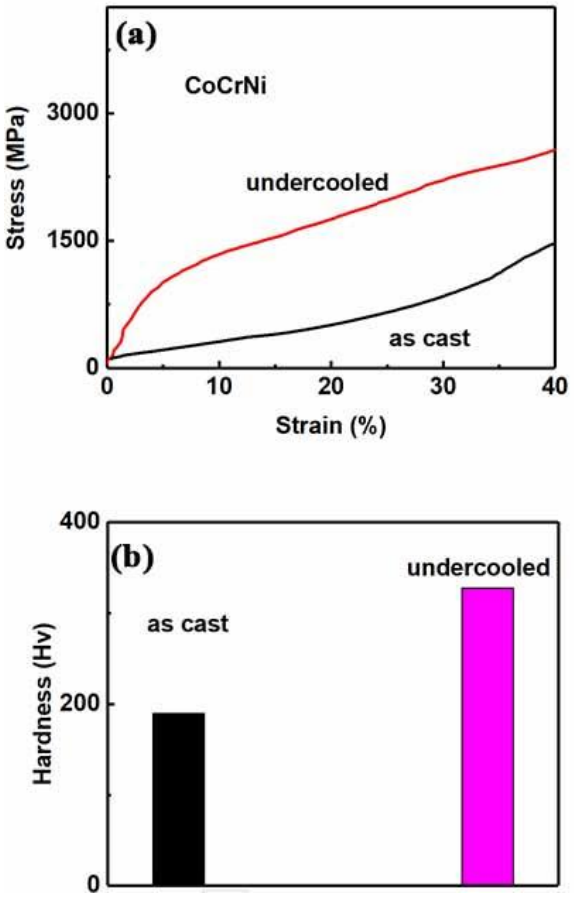

Figure 4 Mechanical properties curves of CoCrNi MEA. (a) The compression curves of CoCrNi MEAs at as-cast and undercooled conditions, (b) Vickers hardness

of CoCrNi MEAs at as-cast and undercooled conditions

4 Conclusions

In summary, the as-cast ternary CoCrNi medium entropy alloy is a single FCC structure, which has evolved into the dendrite structure with hexagonal precipitates in the matrix after undercooling treatment, and the grain size is obviously refined. The Vickers hardness of CoCrNi alloy increased from 183 to 328 HV, and the yield strength increased from 180 to 900 MPa. The grain refinement together with nanometer phase precipitation is the main reason for the increase of mechanical strength of those ternary medium entropy alloy.

Acknowledgment

The support of this work was from National Key R&D Program of China (Grant No: 2022YFA1603800) and the National Natural Science Foundation of China (Grant No: 12274362).

References

[1] J.W. Yeh. Recent progress in high-entropy alloys. European Journal of Control [J]. 2006(31): 633-648.

[2] J.W. Yeh, S.K. Chen, S.J. Lin, et al. Nanostructured high-Entropy alloys with multiple principal elements: novel alloy design concepts and outcomes. Advanced Engineering Materials [J]. 2004(6): 299-303.

[3] Y. Zhang, T.T. Zuo, Z. Tang, et al.. Microstructures and properties of high-entropy alloys. Progress in Materials Science [J]. 2014(61): 1-93.

[4] B. Cantor, I.T.H. Chang, P. Knight. Microstructural development in equiatomic multicomponent alloys. Materials Science and EngineeringA [J]. 2004(213): 375-377.

[5] J.W. Yeh, S.J. Lin, T.S. Chin. Formation of simple crystal structures in Cu-Co-Ni-Cr-Al-Fe-Ti-V alloys with multiprincipal metallic elements. Metallurgical and Materials Transactions A [J]. 2004(35): 2533-2536.

[6] C.J. Tong, Y.L. Chen, J.W. Yeh, et al.. Microstructure characterization of Al_xCoCrCuFeNi high-entropy alloy system with multiprincipal elements. Metallurgical & Materials Transactions A [J]. 2005(36): 881-893.

[7] B.S. Murty, J.W.; Yeh, et al.. Chapter 1–A Brief History of Alloys and the Birth of High-Entropy Alloys.M.Boston：Butterworth-Heinemann Press [D], 2014.

[8] M.R. Chen, S.J. Lin, J.W. Yeh, et al.. Effect of vanadium addition on the microstructure, hardness, and wear resistance of Al0.5CoCrCuFeNi high-entropy alloy. Metallurgical and Materials Transactions A [J]. 2006(37): 1363-1369.

[9] P.K. Huang, J.W. Yeh, T.T. Shun, et al.. Multi-principal-element alloys with improved oxidation and wear resistance for thermal spray coating. Advanced Engineering Materials [J]. 2004(6): 74-78.

[10] A. Poulia, E. Georgatis, A.E. Lekatou, et al.. Microstructure and wear behavior of a refractory high entropy alloy. International Journal of Refractory Metals and Hard Materials [J]. 2016(57): 50-63.

[11] M.D. Zhang, L.J. Zhang, J.T. Fan, et al.. Novel Co-free CrFeNiNb0.1Tix high-entropy alloys with ultra high hardness and strength, Materials Science & Engineering A [J], 2019,764(9): 138212-138221.

[12] W.Q. Dong, Z. Zhou, M.D. Zhang, et al.. Applications of high-pressure technology for high-entropy alloys: A review, Metals, 2019(9): 867.

[13] X. M. Liu, J. T. Fan, X. S. Liu, et al.. Nonlinear vibration of Al-Al based high entropy alloy circular sandwich panel, AIP Advances, 2019, 9(3): 035351.

[14] J. T. Fan, L. J. Zhang, G. Li, et al.. A novel high-entropy alloy with dendrite-composite microstructure and remarkable compression performance, Scripta Materialia, 2019(159): 18–23.

[15] Y. Shi, B. Yang, P.K. Liaw, Corrosion-Resistant High-Entropy Alloys: A Review.J. Metals - Open Access Metallurgy Journal.2017(7): 43.

[16] X. S. Liu, R. Li, X.F. Fan, et al.. Excellent strength-ductility combination in Co36Cr15Fe18Ni18Al8Ti4Mo1 multi-principal element alloys by dual-morphology B2 precipitates strengthening，Journal of Materials Science & Technology [J]. 2023(134): 60–66.

[17] A.X. Li, P.F. Yu, Y.P. Gao, et al.. Ultra-high strength and excellent ductility high entropy alloy induced by nano-lamellar precipitates and ultrafine grain structure, Materials Science & Engineering A [J]. 2023(862): 14428.

[18] D.B. Miracle, O.N. Senkov. A critical review of high entropy alloys and related concepts. Acta Materialia [J].2017(122): 448-511.

[19] M.H. Jiang, Y.P. Gao, Y.Y. Wang, et al.. Study on structure evolution of CoCrFeNi high entropy alloy in containerless processing using neutron differaction, Nuclear Analysis [J]. 2022(3): 100034.

[20] Z. Wu, H. Bei, G.M. Pharr, et al.. Temperature dependence of the mechanical properties of equiatomic solid solution alloys with face-centered cubic crystal structures. Acta Materialia [J]. 2014(81): 428-441.

[21] C. Niu, A.J. Zaddach, A.A. Oni, et al.. Spin-driven ordering of Cr in the equiatomic high entropy alloy NiFeCrCo. Applied. Physics. Letter [J].2015(106): 161906.

[22] D.M. Herlach, Non-equilibrium solidification of undercooled metallic melts. Advances in Space Research [J].1991(12): 177.

[23] C. Suryanarayana, Phase formation under non-equilibrium processing conditions: rapid solidification processing and mechanical alloying. Journal of Materials Science [J]. 2018(53): 13364-13379.

[24] X. Bai, Y. Wang, C. Cao, Metastable phase separation and rapid solidification of undercooled $Co_{40}Fe_{40}Cu_{20}$ alloy. Chinese Physics B [J]. 2018(27): 305-309.

[25] A. Munitz, A. Venkert, P. Landau, et al.. Microstructure and phase selection in supercooled copper alloys exhibiting metastable liquid miscibility gaps. Journal of Materials Science [J]. 2012(47) 7955-7970.

[26] J.H. Perepezko. Solidification of highly supercooled liquid metals and alloys. Journal of Non-Crystalline Solids [J]. 1993(2): 463-472.

[27] J.H. Perepezko, G. Wilde. Amorphization and alloy metastability in undercooled systems. Journal of Non-Crystalline Solids [J]. 2000(274): 0-281.

[28] T. David. Kinetics of Solidification of Supercooled Liquid Mercury Droplets. Journal of Chemical Physics [J]. 1952(20): 411-424.

[29] J.S. Li, W.J. Jia, J. Wang, et al.. Enhanced mechanical properties of a CoCrFeNi high entropy alloy by supercooling method. Materials and Design [J].2016(95): 183–187.

[30] R. Li, X.S Liu, P.F. Yu, et al.. Unveiling the phase evolution and mechanical properties of Ni1.5Co1.5CrTix alloy composites with ultrafine/nano structure, Materials and Design [J]. 2022(223): 111165

[31] L.L. Lacy, M.B. Robinson, T.J. Rathz. Containerless undercooling and solidification in drop tubes. Journal of Crystal Growth [J]. 1981(51): 47-60.

[32] W.H. Hofmeister, M.B. Robinson, R.J. Bayuzick. Undercooling of pure metals in a containerless, microgravity environment. J. Applied Physics Letters [J]. 1986(49): 1342-1344.

[33] J.S. Li, W.J. Jia, J. Wang, et al.. Enhanced mechanical properties of a CoCrFeNi high entropy alloy by supercooling method. Materials & Design [J]. 2016(95): 183-187.

[34] A.M. AMullis, P.C. Bollada, P.K. Jimack, Phase-Field Modelling of Intermetallic Solidification. M. TMS 2018 147th Annual Meeting & Exhibition Supplemental Proceedings [D], 2018.

[35] Y.L. Liu, L. Luo, Z.S. Ming, et al.. Microstructure and mechanical properties of Al-5.5Fe-1.1V-0.6Si alloy solidified under near-rapid cooling and with Ce addition. Rare Metals [J]. 2018(12): 1070-1075.

[36] J. Wang, T. Guo, J. Li, et al.. Microstructure and mechanical properties of non-equilibrium solidified CoCrFeNi high entropy alloy. Materials Chemistry and Physics [J]. 2018(210): 192-196.

[37] X. Hao, Y.G. Li, Y. Hu, et al.. Effect of the Third Element Ni on the Solidification Microstructure of Undercooled Cu-40 wt.% Pb Monotectic Alloy Melt. Advances in Materials Science and Engineering [J]. 2019(2): 1-7.

[38] J. Wang, G. Tong, J. Li, et al.. Microstructure and mechanical properties of non-equilibrium solidified CoCrFeNi high entropy alloy. Materials Chemistry and Physics [D], 2017.

[39] R.D. Li, P.D. Niu, T.C. Yuan, et al.. Selective laser melting of an equiatomic CoCrFeMnNi high-entropy alloy: Processability, non-equilibrium microstructure and mechanical property. Journal of Alloys and Compounds: An Interdisciplinary Journal of Materials Science and Solid-state Chemistry and Physics [D], 2018.

[40] Q. Gao, X.S. Jiang, H.L. Sun, et al.. Effect mechanism of cryogenic treatment on ferroalloy and nonferrous alloy and their weldments: a review. Materials Today Communications [J]. 2022(1): 104830.

[41] X.W. Hong, C.H. Hsueh. Effects of yttrium addition on microstructures and mechanical properties of CoCrNi medium entropy alloy. Intermetallics [J]. 2022(140): 107405.

[42] H.W. Deng, Z.M. Xie, B.L. Zhao, et al.. Tailoring mechanical properties of a CoCrNi medium-entropy alloy by controlling nanotwin-HCP lamellae and annealing twins. Materials Science and Engineering [J]. 2019(744): 241-246.

[43] J.P. Liu, J.X. Chen, T.W. Liu, et al.. Superior strength-ductility CoCrNi medium-entropy alloy wire. Scripta Materialia [J].2020(181): 19-24.

[44] B. Gwalani, T. Torgerson, S. Dasari, et al.. Influence of fine-scale B2 precipitation on dynamic compression and wear properties in hypo-eutectic Al0.5CoCrFeNi high-entropy alloy. Journal of Alloys and Compounds: An Interdisciplinary Journal of Materials Science and Solid-state Chemistry and Physics [J]. 2021, 853(1): 5.

[45] Z.Y. Jia, S.Z. Zhang, J.T. Huo, et al.. Heterogeneous precipitation strengthened non-equiatomic NiCoFeAlTi medium entropy alloy with excellent mechanical properties. Materials Science and Engineering [J]. 2022(834):142617.

[46] L. Zhang, X. Du, L. Zhang, et al.. Achieving ultra-high strength in a precipitation-hardened CoCrNi-based medium-entropy alloy with partially recrystallized microstructure and heterogeneous grains [J]. Vacuum, 2021, 188(28):110169.

Viser Technology Pte. Ltd.
Research and Application of Materials Science
DOI: 10.33142/rams.v4i2.8465

Research Article Open Access

The effect of binder phase content on WC-AlCoCrFeNiTi$_{0.2}$ high entropy cemented carbides microstructure and mechanical properties

Yuxin WEN[1], Mingchen ZHANG[2], Yong ZHANG[1*]

1 State Key Laboratory for Advanced Metals and Materials, University of Science and Technology Beijing, Beijing 100083, China
2 Inspection and Certification Co., Ltd., MCC, Beijing 100088, China

***Corresponding Author:** drzhangy@ustb.edu.cn*

Abstract:
This work aims to explore WC-G201 high entropy cemented carbides properties fabricated by spark plasma sintering with AlCoCrFeNiTi$_{0.2}$ and WC as binder phase and hard phase respectively. AlCoCrFeNiTi$_{0.2}$ powder and WC powder were mixed at the mass ratio of 5: 95, 10: 90 and 15: 85 respectively, and then via SPS at 1300℃ for 5min. The results show that the binder phase has good wettability to WC, and with the increase of binder phase content, the hardness of the alloy decreases gradually, fracture toughness increases first and then decreases, the maximum value is 7.88 MPa m$^{1/2}$. It is estimated that the comprehensive mechanical property of cemented carbides is the best when the binder content is between 5wt% and 10wt%.
***Keywords:** High entropy alloys; cemented carbides; binder phase*

1 Introduction

Cemented carbides is an alloy material synthesized by powder metallurgy technology with hard refractory carbides powder and Co, Ni or other adhesive powders as the binder phase [1]. Owing to its excellent hardness, wear resistance, corrosion resistance and oxidation resistance, it is widely used in tools, molds and other fields [2]. At present, WC is mostly used as the hard phase and Co as the adhesive phase, but this cemented carbide has some shortcomings such as poor oxidation resistance at high temperature, Co is unhealthy due to toxic, and it is very scarce in our country, there are some disadvantages such as the difficulty of extracting and the high price of Co [3]. Therefore, it is particularly important to find a new binder phase that can replace Co binder.

High entropy alloy is a kind of solid solution structure composed of multiple components. High entropy alloy has become a research hotspot, due to the crystal structure of high entropy alloy brings some excellent performances, such as high strength, high wear resistance and thermal stability [4-8], generally the softening resistance temperature of traditional tool steel is less than 550℃ [9]. Some scholars [10] found that the hardness of FeCoNiCuAl high-entropy alloy can still keep 532HV above after annealing at 1000℃ for 5h, showing excellent high temperature hardness. The good wettability of the binder phase to the hard phase is the premise that the alloy can be applied to the binder phase of the cemented carbides. It has been found that the high entropy alloy has good wettability and can inhibit the ceramic grain growth. If the equilibrium contact angle is between 0 and 30°, it is considered to have good wettability. Luo et al.[11] studied the wettability of Al$_x$CoCrCuFeNi (x=0, 0.5, 1, 1.5) on WC, and measured the size of the equilibrium contact angle as 0.5°, 0.9°, 2.0° and 4.6° respectively, which research has enabled scholars to discover the potential of high entropy alloys as cemented carbide. Zhou Panlong et al. [12] used Al$_x$CrFeCoNi high entropy alloy as the binder phase to produce high entropy cemented carbides with tungsten carbide as matrix. The mechanical property test found that cemented carbides had higher hardness than traditional WC-10Co cemented carbides, and also had good fracture toughness. In summary, it can be seen that it is feasible to select the high entropy alloy as the binder phase. High entropy alloys with the right elements as binder phases can improve the mechanical properties of cemented carbides. Studies have found that Al, Co, Fe, Ni and their intermetallic compounds have good wettability to WC. Zhou Yunjun et al. [13] studied the effect of Ti content on AlCoCrFeNiTi$_x$ (x=0, 0.5, 1, 1.5), after the Ti was added, the lattice distortion of the alloy was aggravated, it caused solution strengthening and nanophase diffusion strengthening, thereby improving the strength and hardness of the alloy. The yield strength

Received on November 18, 2022; Accepted on December 20, 2022

of the alloy system is higher than 1.5 GPa, the breaking strength is higher than 2.5 GPa, and the plastic deformation is as high as 23.22%. Later Zhang Yong research group found that when x = 0.2 in $AlCoCrFeNiTi_x$, the strength and plasticity of the alloy have been improved, it shows excellent mechanical properties. Therefore, $AlCoCrFeNiTi_{0.2}$ was selected as the binder phase.

The three most commonly used methods for preparing high entropy cemented carbide are vacuum sintering, vacuum hot pressing sintering and spark plasma sintering (SPS). Yang Mei et al. used SPS to prepare high entropy cemented carbides, which overcame the problem of mechanical properties deteriorated due to the excessively growth of WC grains [14]. Dai Pinqiang et al. sintered WC-FeCoCrNiAl high entropy cemented carbides by using these three methods respectively, and found that the hardness of cemented carbides by SPS was the highest, reaching 1900 HV [15]. SPS has the characteristics of short sintering time to inhibition of grain growth, so that it can reduce the formation of other harmful phases, resulting in excellent mechanical properties of the high entropy cemented carbides.

In this study, The $AlCoCrFeNiTi_{0.2}$ (noted as GS201) [16] was used as the binder phase and WC was used as the hard phase to fabricate high entropy cemented carbides by SPS. The influence of the binder phase content of GS201 on the microstructure and mechanical properties of high entropy cemented carbides was studied.

2 Materials and methods

GS201 high-entropy alloy powder prepared by WLL-100 vacuum atomization equipment was used in the experiment. Figure1 shows the morphology of GS201 powder. Tungsten carbide-powder was purchased from Hebei Jiuyue New Material Technology Co., Ltd.

High entropy alloy powder and tungsten carbides powder were mixed for 6h with 200rpm in the SFM-2 vertical planetary mixer at the ratio of 5: 95, 10: 90 and 15: 85 respectively. After the mixed progress, the powder was dried at 80℃ in a vacuum drying oven for 24h. Then 40g of dried powder was sintered in SPS-20T-10-III spark furnace. The sintering process is as follows: when the vacuum degree is maintained below 10^{-3}Pa, the temperature is raised to 650℃ at 100℃/min, the heat is kept for 5min, and then the pressure is increased to 30MPa. Then the temperature is raised to 1200℃ at 100℃/min, and the temperature is increased to 1300℃ at 50℃/min, and the sintering is performed for 5min. Figure2 is the prepared high entropy cemented carbides, from left to right it is WC-5wt%GS201, WC-10wt%GS201 and WC-15wt%GS201.

The melting point of high entropy alloys was tested using equipment of the German company Netzsch model DSC404F1. The contact angle measurement instrument of OCA25-HTV1800 of Data physics was used to measure the contact angle between GS201 and WC at high temperature. The phase analysis was carried out by Rigaku Smart Lab diffractometer. The surface and cross section morphologies of high entropy cemented carbides samples were observed by using ZEISS SUPRA55 field emission scanning electron microscope and Olympus 3D laser measuring microscope model LEXT OLS4100. 430SVD Walport (Shanghai) digital hardness tester was used for hardness test. The fracture toughness of cemented carbides was calculated by indentation method according to Vickers indentation. According to GB/T2997-2000, the Archimedes principle is used to measure the actual density of the sample, and then the relative density of the high entropy cemented carbides is calculated.

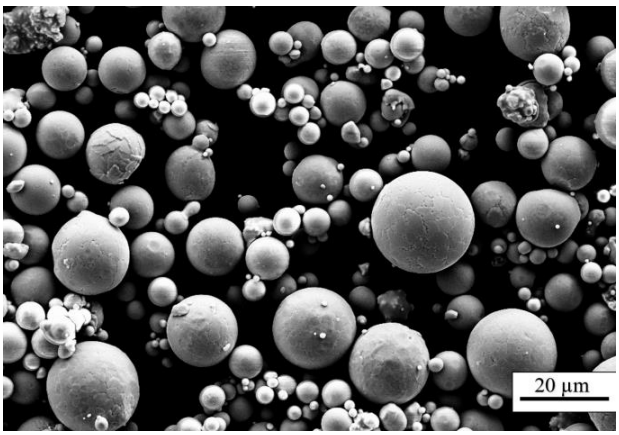

Figure 1 Morphology of GS201 powder

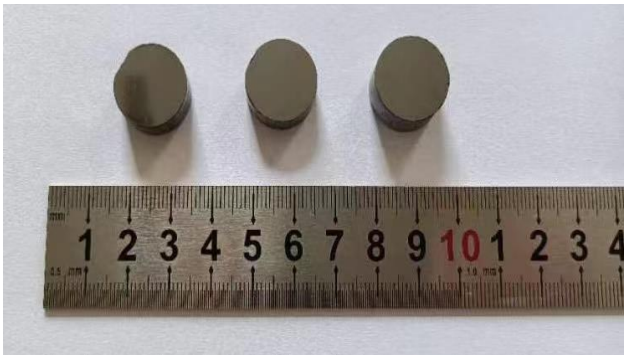

Figure 2 High entropy cemented carbides blocks

3 Results

3.1 Analysis of the wetting ability of GS201 to WC

Figure 3 shows the DTA curve of GS201. It can be seen from the figure that the melting point of GS201 is 1312.79℃, there are two endothermic peaks at 650℃ and 1000℃, which should be due to phase transition. GS201 completely melted at 1368℃, therefore, when studying the wettability of GS201 to WC, the sintering temperature should be increased to more than 1358℃. It provides a reference for the temperature setting of our wetting experiment.

Figure 4 shows the contact angle between GS201 and WC at high temperature. Before the temperature rises to 1368℃, the high entropy alloy block does not melt, and the contact angle between the high entropy

alloy and tungsten carbides remains 90 ° as shown by (a) in Figure 5 When the temperature rises to 1368℃, both sides of the block gradually bend outward with a curved profile. The contact angle increases and reaches a maximum of 130 ° at 1376℃. With the temperature rise continuously, the alloy block began to melt and spread, and the spreading speed accelerated at 1378℃. When the temperature rose to 1380℃ within 1 min, the contact angle rapidly decreased to 33 °. Subsequently, the melting rate of the high entropy alloy block slows down, and the change rate of the wetting Angle decreases correspondingly. After 7 min, the temperature rises to 1400℃, and the contact Angle decreases to 16.5 °, as shown in Figure5 (c). After the temperature rises to 1408℃ within 9 min, the contact angle decreases to 3.8 °. As the temperature further rises to 1420℃, the contact angle is basically unchanged, decreasing from 3.8 ° to 3.4 °. When the temperature is kept at 1420℃ for 20 min, the contact angle is almost unchanged, as shown in Figure4, which is between 3.3 °and 3.4 °, as shown in Figure5 (d). The results analysis shows that GS201 has excellent wettability to WC and meets the requirements of cemented carbides with binder phase.

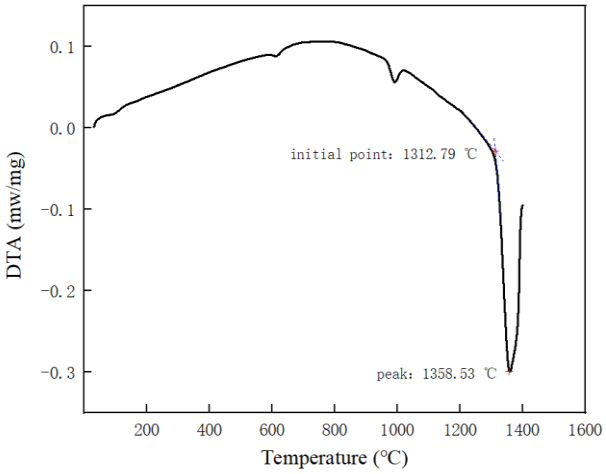

Figure 3 The DTA data graph of GS201

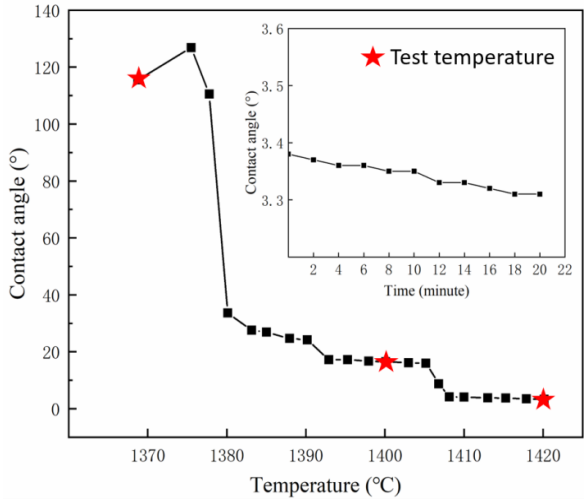

Figure 4 Changes of antennae of GS201 on WC with temperature and time

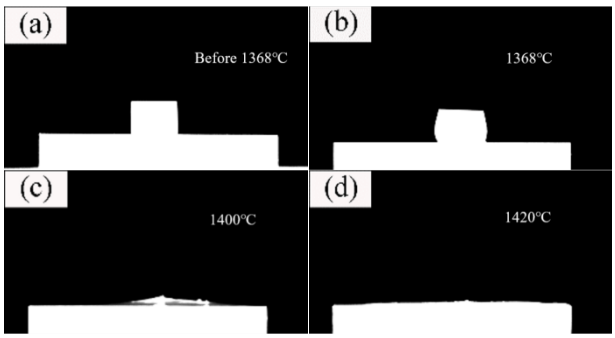

Figure 5 Profile of WC wetting process of GS201

3.2 Phase analysis and microstructure morphology analysis of WC-AlCoCrFeNiTi0.2 high entropy cemented carbides

Figure6 shows the XRD pattern of high entropy cemented carbides with different contents of GS201 at the sintering temperature of 1300℃. There are only diffraction peaks of WC and GS201 in WC-5wt%GS201. With the increase of GS201 content, diffraction peaks of unknown phases (denoted as γ phase) appear at about 41°. γ phase is the most obvious in WC-15wt%GS201. It could be that when the content of GS201 is higher than a certain value, WC will react with some elements of GS201 to form intermetallic compounds. Under this specific value, GS201 can exist stable after SPS sintering.

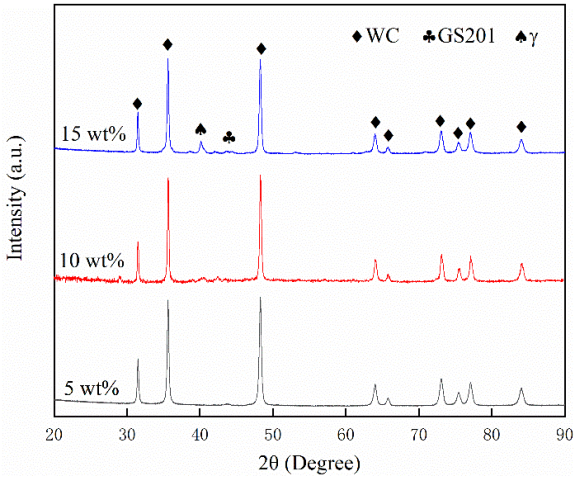

Figure 6 XRD pattern of WC-GS201 after sintering at 1300℃

Figure 7 shows the microstructure of WC-5wt%GS201, WC-10wt%GS201 and WC-15wt%GS201 high entropy cemented carbides sintered at 1300℃. In the figure, gray is tungsten carbides grains, with smooth grain profiles and wide grain size distribution range. The black material is GS201 binder phase. In WC-5wt%GS201, GS201 binder phase is not fully filled in the grain gap of WC, and there are still pores. With the increase of the binder phase content, the WC grain gap was gradually fully filled. When the binder phase content increased to 15%, a new dark gray substance was found in the WC grain gap, which should be the new phase generated by the

reaction of WC and GS201, which was consistent with the results of the unknown phase at about 41° in the XRD analysis above.

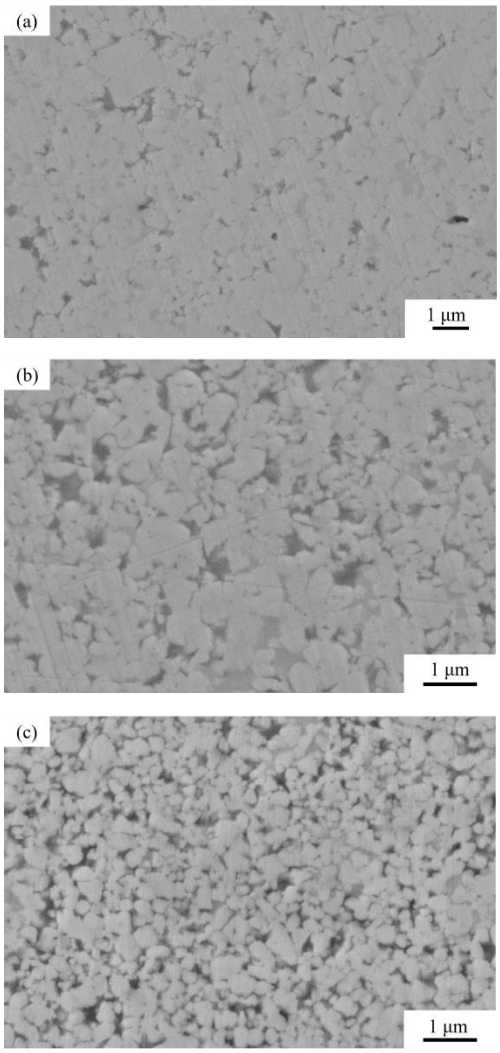

Figure 7 Microstructure of WC-GS201 high entropy cemented carbides

(a), (b) and (c) are cemented carbides with binder phase content of 5wt%, 10wt% and 15wt% sintered at 1300℃, respectively.

3.3 Grain size analysis of WC-GS201 high entropy cemented carbides

The growth of WC grains follows Ostwald theory [17], which progress can be divided into three stages: (1) dissolution of WC grains at high temperature, (2) precipitation of dissolved WC grains with the decrease of temperature, and (3) WC grains grow up. The process of WC grain growth combines with the continuous dissolution and precipitation of W and C elements. According to the BSE image of WC-GS201 high entropy cemented carbides, the average grain size of tungsten carbides is calculated with Image software, and the calculation results are shown in Figure8 WC-5wt% GS201 has the largest grain size of 0.61μm. The grain size of WC-15wt% GS201 is the smallest, which is 0.33μm, indicating that the binder phase of GS201 inhibits the growth of WC grains, but this inhibition is not linearly related to the binder phase content. With the increase of binder phase content, the inhibition effect on grain growth is gradually enhanced, and the grain size of WC decreases gradually.

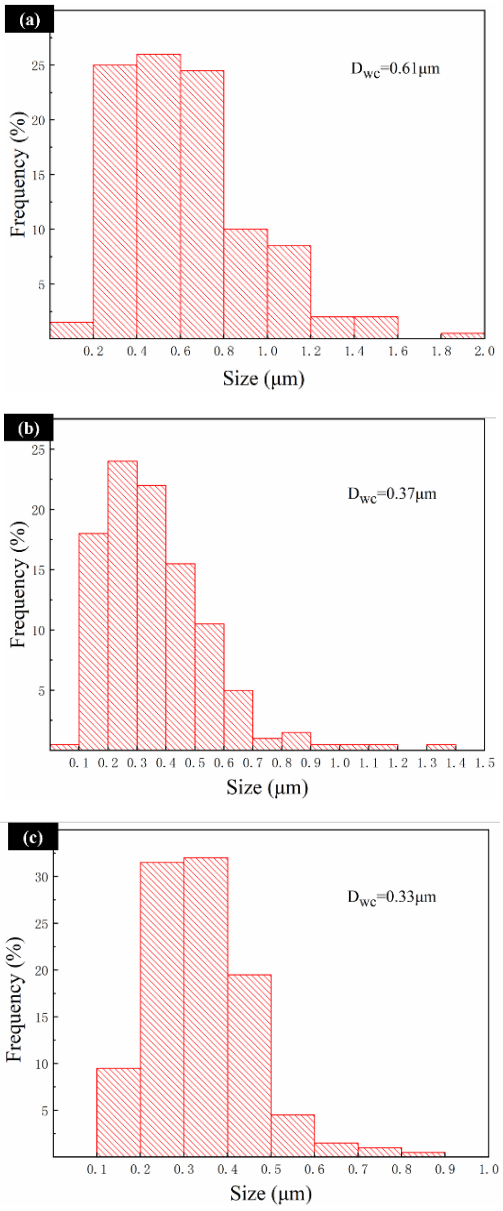

Figure 8 Grain size distribution of WC-GS201 high entropy cemented carbides

(a), (b) and (c) are cemented carbides with binder phase content of 5wt%, 10wt% and 15wt% sintered at 1300℃

3.4 Analysis of relative density and mechanical properties of WC-GS201 high entropy cemented carbides

Figure 9 shows the density and relative density of WC-GS201 at the sintering temperature of 1300℃. With the increase of GS201 binder phase content, the relative density of high entropy cemented carbides gradually increases. Through the microstructure analysis, 5wt% GS201 binder phase did not completely

fill the gap between WC grains, resulting in direct contact or gaps between WC grains, so the relative density is relatively low. Under the effect of high temperature and pressure, the liquid binder with sufficient content flows quickly to the grain space and then solidifies, and the internal defects (such as voids) of the material are reduced and the relative density is increased. When the content of adhesive phase is 10wt% and 15wt %, the relative density is both greater than 99%, indicating that the gap of WC grains at this time has been fully filled, which is consistent with the microscopic morphology observed under scanning electron microscopy. GS201 and WC grains have good wettability, meeting the requirements for adhesive phase. The relative density value reflects the internal defects of the material. The higher the relative density of the alloy, resulting from the fewer defects such as pores inside the alloy, facilitate the mechanical properties of the alloy promotion.

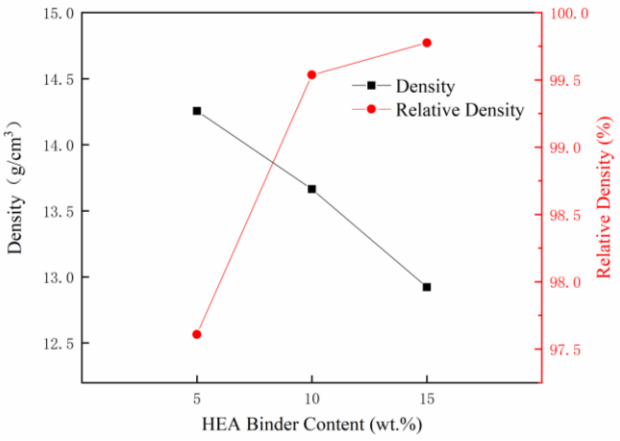

Figure 9 Relationship between the relative density of WC-GS201 after sintering at 1300℃ and the content of bond phase

Figure 10 shows the relationship between the hardness and fracture toughness of WC-GS201 high entropy cemented carbides sintered at 1300℃ and the content of bond phase. With the increase of binder content, Vickers hardness decreases gradually. When the binder content increases from 5wt% to 10wt%, the hardness of alloy decreases from 1568 HV_{30} to 1368 HV_{30}. According to the above grain size analysis, the grain size decreases and the hardness of the alloy increases with the increase of the cohesive phase content. The high hardness of hard phase is also the reason for the high hardness of high entropy cemented carbides. The results show that with the decrease of hard phase content, the overall hardness of the alloy decreases accordingly. In summary, it can be seen that the effect of the decrease of hard phase content on the decrease of alloy hardness is greater than the effect of fine crystal strengthening on the increase of hardness, so the overall hardness of the alloy shows a decreasing trend. The fracture toughness of the alloy increases first and then decreases, and the maximum value is 7.88MPa $m^{1/2}$.

Figure 11 shows the SEM image of the indentation crack of WC-GS201. The red arrow marks the crack deflection, the yellow circle marks the crack bridging, the blue arrow marks the grain pulling out, and the white arrow marks the transcrystal fracture, all of which will enhance the fracture toughness of the alloy [18][19]. The reason is that the fracture toughness is related to the resistance encountered during crack propagation. The greater the resistance it is, the higher the fracture toughness will be. When the binder phase content is 5wt%, the crack is relatively gentle; when the binder phase content is increased to 10wt%, the relative density of the alloy increases, and the transgranular fracture and crack deflection increase, which consumes a lot of energy during fracture and improves the fracture toughness of the alloy [20]. When the binder phase content increased to 15wt%, the relative density slightly increased, but the fracture toughness decreased. Combined with the XRD analysis above, the unknown corresponding brittle phase was generated, thus reducing the fracture toughness of the alloy. The alloy has the best comprehensive mechanical property when the binder phase content is between 5wt% and 10wt%. Combined with XRD and relative density analysis, with the increase of binder phase content, when the relative density reaches 99%, it can be regarded as the binder phase has been fully filled in the WC grain gap, and no other intermetallic compounds are formed at this time, namely no new phase appears in XRD. At this time the comprehensive mechanical properties of the alloy should be the best.

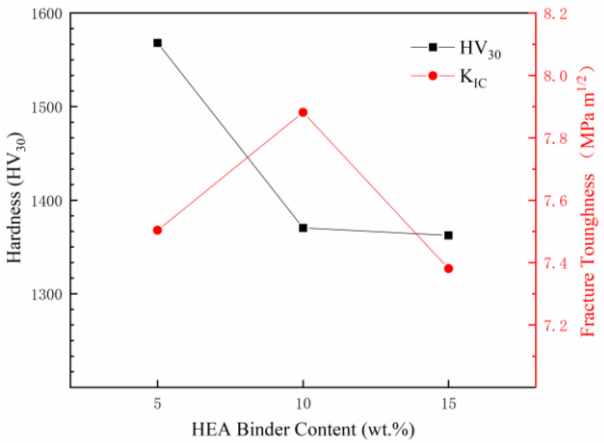

Figure 10 Relationship between hardness and fracture toughness of WC-GS201 sintered at 1300℃ and bond phase content

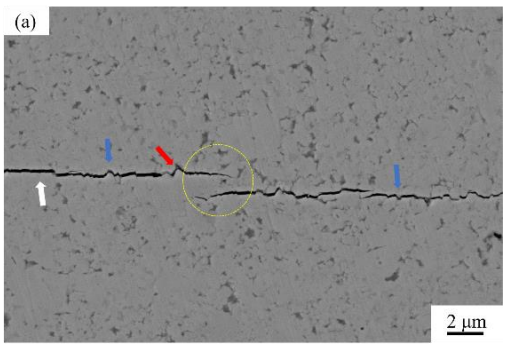

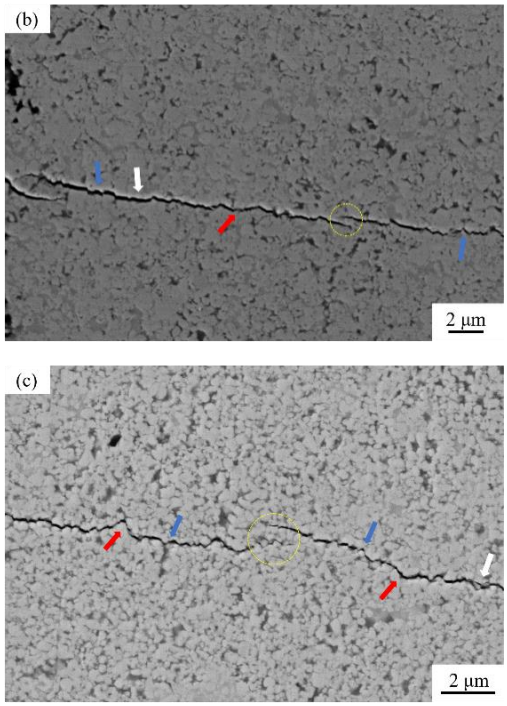

Figure 11 SEM image of the indentation crack of WC-GS201

4 Conclusions

(1) GS201 has excellent wettability to WC. The high temperature contact angle between GS201 and WC is between 3.3° and 3.4° at 1420℃ respectively, meeting the requirements of cemented carbides for adhesive phase.

(2) With the increase of the binder content, the Vickers hardness of the alloy decreases gradually, and the influence of the hardness of the cemented carbides is greater than that of the fine hardening. The fracture toughness increases first and then decreases, and the maximum value is 7.88MPa $m^{1/2}$. The optimal comprehensive mechanical property should be a value of binder phase content between 5wt% and 10wt%.

References

[1] Yang J G, Dai Y. Development trend of cemented carbides and preparation technology of special powder [J]. Rare metals and hard metals, 2011(1): 48-51.

[2] Chu K Y. Development status and prospect of Chinese cemented carbides industry [J]. Rare metals and hard metals, 2011, 39(1): 52-56.

[3] Kim H C, Shon I J, Garay J E, et al.. Consolidation and properties of binderless sub-micron tungsten carbide by field-activated sintering [J]. International Journal of Refractory Metals and Hard Materials, 2004, 22(6): 257-264.

[4] Ji W, Wang W, Wang H, et al.. Alloying Behavior and Novel Properties of CoCrFeNiMn High-Entropy Alloy Fabricated by Mechanical Alloying and Spark Plasma Sintering [J]. Intermetallics, 2015(56): 24-27.

[5] Tong C J, Chen M R, Yeh J W, et al. Mechanical Performance of The $Al_xCoCrCuFeNi$ High-Entropy Alloy System with Multiprincipal Elements [J]. Metallurgical and Materials Transactions A, 2005, 36(5): 1263-1271.

[6] Varalakshmi S, Rao G A, Kamaraj M, et al.. Hot Consolidation and Mechanical Properties of Nanocrystalline Equiatomic AlFeTiCrZnCu High Entropy Alloy after Mechanical Alloying [J]. Journal of materials science, 2010, 45(19): 5158-5163.

[7] Song X F, Zhang Y. Research progress of high entropy alloys [J]. Powder Metallurgy Technology, 2022, 40(5): 451-457.

[8] Zhang Y. Discovery and development of high entropy alloys [J]. Journal of Sichuan Normal University, 2022, 45(6): 711-722.

[9] Kwak B W, Song J H, Kim B S, et al.. International Journal of Refractory Metals and Hard Materials, 2016(54): 244-250.

[10] Zhuang Y X, Xue H D, Chen Z Y, et al.. Effect of Annealing Treatment on Microstructures And Mechanical Properties of FeCoNiCuAl High Entropy Alloys[J]. Materials Science and Engineering: A, 2013(572): 30-35.

[11] Luo W Y, Liu Y Z, Tu C. Wetting behaviors and interfacial characteristics of molten $Al_xCoCrCuFeNi$ high-entropy alloys on a WC substrate [J]. Journal of Materials Science & Technology, 2021(78): 192-201.

[12] Zhou P L, Xiao D H, Zhou P F, et al.. Microstructure and properties of ultrafine crystal WC-$Al_xCrFeCoNi$ composites prepared by hot pressing[J]. Powder metallurgy materials Science and Engineering, 201, 11(30): 95-103.

[13] Zhou Y J, Zhang Y, Wang Y L, et al.. Mechanical properties and strengthening mechanism of $Ti_xCrFeCoNiAl$ multicomponent solid solution alloy system [J]. Chinese Journal of Materials Research, 2008 (5):461-466.

[14] Yang M, Luo X, Long J P. Chengdu University of Technology. The invention relates to a preparation method of high entropy alloy binder phase cemented carbides. 109161773A[P]. 2019-01-08.

[15] Dai P Q, Liu X Q, Guo K K, et al.. The invention relates to a preparation method of WC - based cemented carbides with high entropy alloy powder as binder: CN201811445236. 0[P]. 2019-02-22.

[16] Wu Y Q, Liaw P K, Zhang Y. Preparation of bulk TiZrNbMoV and NbTiAlTaV high-entropy alloys by powder sintering [J]. Metals, 2021, 11(11): 1748.

[17] García J, Collado Ciprés V, Blomqvist A, et al.. Cemented carbide microstructures: a review [J]. International Journal of Refractory Metals and Hard Materials, 2019(80): 40-68.

[18] Zhou P F, Xiao D H, Yuan T C. Comparison between ultrafine-grained WC-Co and WC-HEA-cemented carbides [J]. Powder Metallurgy, 2017, 60(1): 1-6.

[19] Fu Z, Koc R. TiNiFeCrCoAl high-entropy alloys as novel metallic binders for TiB2-TiC based composites [J]. Materials Science and Engineering a-Structural Materials Properties Microstructure and Processing, 2018(735): 302-309.

[20] Ji W, Zhang J Y, Wang W M, et al.. Fabrication and properties of TiB_2-based cerments by spark plasma sintering with CoCrFeNiTiAl high-entropy alloy as sintering aid [J]. Journal of the European Ceramic Society, 2015, 35(3): 879-86.

Viser Technology Pte. Ltd.
Research and Application of Materials Science
DOI: 10.33142/rams.v4i2.8466

Research Article Open Access

Effect of electric pulse rolling on plastic forming ability of AZ91D magnesium alloy

Xinyu LIU[1], Yuezhang ZHOU [1], Wenjie BO [1], Yong ZHANG [2], Guihong GENG [1*]

1 School of Materials Science and Engineering, North Minzu University, Yinchuan 750021, P.R. China
2 State Key Laboratory for Advanced Metals and Materials, University of Science and Technology Beijing, Beijing 100083, China.

***Corresponding Author:** Guihong GENG, E-mail: gengguihong@nmu.edu.cn*

Abstract:
AZ91D magnesium alloy rolled under four rolling conditions, namely cold rolling, electric pulse cold rolling, hot rolling and electric pulse hot rolling, and the first principles calculation of Mg with or without external electric field carried out. The results show that: The application of pulse current in the rolling process of AZ91D magnesium alloy can effectively improve the edge crack of the sample, optimize the texture of AZ91D magnesium alloy and reduce its texture strength, promote the generation of tensile twins and the transition from small Angle grain boundaries to large Angle grain boundaries, and thus improve the plastic forming ability of AZ91D magnesium alloy. Make it more prone to plastic deformation. Compared with ordinary rolling, the microhardness of α-Mg matrix decreases by 15%. The tensile strength and elongation increased from 137MPa and 3.4% to 169MPa and 4.7%, respectively. The results show that the stiffness of Mg decreases and the Poisson's ratio of Mg increases when the electric field applies. When the B/G value is greater than 1.75, the plasticity of Mg is improved. The fault energy at the base surface of Mg does not change much, while the fault energy at the prismatic surface of Mg decreases obviously, showing the external electric field mainly affects the prismatic surface slip of Mg, which makes the prismatic surface slip easier to start, and thus improves the plastic forming ability of Mg.
***Keywords:** Electric pulse rolling; Electroplasticity; AZ91D; First principles calculation*

1 Introduction

Magnesium alloy has become one of the lightweight process materials in the new century due to its high specific strength and stiffness, low density, good electrical and thermal conductivity, and good damping and shock absorption [1-2]. Its structural parts have wide application prospects in automotive, aerospace, and communication fields [3-5]. However, magnesium metal belongs to the dense row hexagonal crystal structure, only the base plane ＜a＞ can open the slip at room temperature [6], so its room temperature deformation ability is poor, it is difficult to carry out mass industrial production by cold deformation, which greatly limits the application of magnesium alloy in industry, so magnesium alloy mostly adopts the method of hot forming [7]. However, under hot forming conditions, there are problems such as reduced die life, roughness of magnesium alloy surface, increased thermal stress of magnesium alloy and higher energy consumption [8].

In recent years, it has shown the application of certain pulsed currents during the deformation of metallic materials can effectively improve their plastic forming ability, a phenomenon known as the electroplastic effect. Indhiarto et al [9] performed unidirectional tensile experiments on AZ31B magnesium alloy by applying pulsed currents with different peak current densities at the same temperature. The results showed the ultimate tensile strength gradually decreases with increasing peak current density, independent of temperature. This proves that the non-thermal effect of pulsed current has a positive effect on the tensile properties. Liu et al [10] conducted tensile tests on AZ31B magnesium alloy sheet with different frequencies of pulsed current and showed the pulsed current did not change the initial yield stress of the magnesium alloy, but reduced the work-hardening rate and produced a softening effect. In addition, the electroplastic effect was controlled by thermal activation. Although the electroplastic effect of magnesium alloys has been studied by a large number of researchers, the mechanism of the action of current on magnesium alloys is still unclear. In 1968 Vitek [11] proposed the concept of generalized layer fault energy and applied it to the calculation of plastic forming ability of magnesium alloys. Yuasa et al [12] calculated the generalized layer fault energy of Mg, Mg-Zn-Ga, Mg-Ga and Mg-Zn. The calculation results showed that the addition of Ca and Zn reduced the plastic anisotropy of magnesium alloys, which was due to the unstable base slip in the alloy due to the nonlinear nature of the layer error energy.

Received on November 4, 2022; Accepted on December 13, 2022

In this paper, AZ91D magnesium alloy rolled under four rolling conditions: ordinary cold rolling (CR), electric pulse cold rolling (EPC-CR), ordinary hot rolling (HR) and electric pulse hot rolling (EPC-HR). EBSD analysis and theoretical calculation performed on AZ91D magnesium alloy after electric pulse rolling to investigate the effect of electric pulse rolling on the plastic forming ability of AZ91D magnesium alloy.

2 Experimental materials and methods

2.1 Experimental materials

Commercial AZ91D magnesium alloy sheet is selected as the experimental material, and its main components are shown in Table 1. The AZ91D magnesium alloy sheet was cut into 60×12×3mm experimental sheet by wire-cutting equipment. The experimental sheet was held at 400℃ for 3h before use, and then completely annealed by air cooling.

Table 1 Main components of AZ91D magnesium alloy

Element	Al	Zn	Mn	Si	Cu	Mg
wt.%	9	0.67	0.25	0.05	0.015	Others

2.2 Electric pulse rolling process of AZ91D magnesium alloy

AZ91D magnesium alloy rolling experiment adopts strong pulse current rolling equipment independently developed by the research group, which is mainly composed of four-roll rolling equipment and strong pulse power supply. Pressure sensors are equipped on the rolls to display the pressure between the upper and lower rolls in real time. The strong pulse rolling equipment and its working principle are shown in Figure 1. The peak current and current frequency in the rolling process can be displayed by the equipment sensor and oscilloscope.

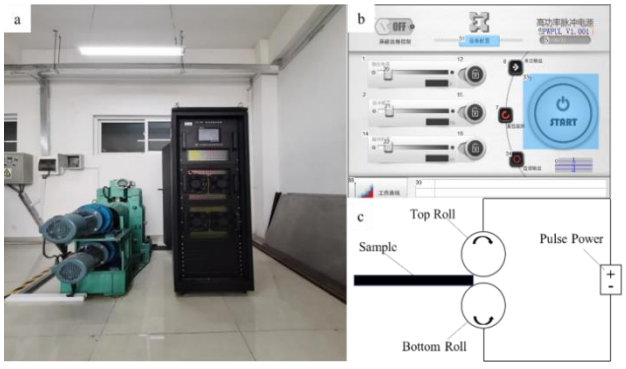

Figure 1 Schematic diagram of high intensity pulse rolling equipment and its working principle: (a) strong pulse rolling equipment, (b) strong pulse power control panel, (c) schematic diagram of electric pulse rolling principle

The specific rolling experimental steps are as follows: (1) use the wire cutting equipment to cut the sample into 60×12×3mm AZ91D magnesium alloy sheet (2) the cut sample will polish off its processing layer with 400# sandpaper and cleaned with ethanol ultrasonic for 5min. (3) the sample to roll will held in 150℃ electric furnace for 10min and then quickly removed for pre-rolling, the amount of pressure down is 1%. (4) the pre-rolled sample will held in 150℃ electric furnace insulation for 10min to remove residual stress, a single pass large amount of depression (20%) electric pulse rolling. The rolling parameters show in Table 2.

Table 2 Rolling parameters

Sample	Voltage (V)	Frequency (Hz)	Pulse width(μs)	Current density(A/mm^2)	Roller temperature(℃)
CR	200	600	20	342	25
EPC-CR	200	600	20	342	27
HR	200	600	20	342	124
EPC-HR	200	600	20	342	119

2.3 Analysis, testing and calculation methods

The samples of AZ91D magnesium alloy after all four rolling processes intercepted from the middle position for testing. The samples polished and electrolytically polished and then analyzed by EBSD using a thermal field emission scanning electron microscope (ZEISS-Sigma 500), where the electrolytic polishing solution was 10% perchloric acid alcohol solution. To further investigate the mechanical properties of AZ91D magnesium alloy after electric pulse rolling, the microhardness test of AZ91D magnesium alloy matrix and Mg17Al12 second phase before and after rolling carried out using HXD-1000TM microhardness tester. The test conducted with an experimental load of 4.9N, a load loading time of 15s, and 10 points for each AZ91D magnesium alloy sample matrix and Mg17Al12 second phase, and the average value of their microhardness taken. CMT5305 type microcomputer-controlled electronic universal testing machine for room temperature tensile performance testing, tensile specimen sample size in line with the GB/T228-2002 calibration selected rectangular equal scale reduction specimens.

The Mg crystal belongs to the dense hexagonal structure, the space point group code is P63/MMC, the lattice constants are A = B =0.3209, C =0.5211, α=β=90°, γ=120°. The Mg crystal model cut, and the Mg base plane thin plate model and prismatic plane thin plate model cut respectively, as shown in Figure 2. Each thin plate model contains 96 atoms, and the thin plate is directly set with a 1.5nm vacuum layer. In this paper, the first-principle method based on density functional theory (DFT) was used for calculation, and the CASTEP module used to optimize and calculate the structure of Mg crystal model. The PBE in generalized Gradient approximation (GGA) used as the exchange correlation functional in calculation. The self-consistent field method (SCF) used to solve the Kohn-Sham equation. Among them, the convergence value of SCF energy is 1.0×10-5 eV/atom. The plane wave cutoff energy is set to 400 eV. The calculated convergence accuracy is 1.0×10-5 eV/atom. The maximum number of self-consistent

iterations is 1000.The maximum convergence accuracy of the force on each atom is 0.01 eV/A. The K Point of the first Brillouin zone was set as 2×4×1. The internal stress convergence standard of the crystal was 0.05 GPa. The external electric field intensity was set as 0.1 eV. The direction was parallel to the Z-axis. The above parameters are used to optimize the geometry of the Mg crystal model. The lattice constants after optimization show in Table 3, and the error between them and the reference value is within 1%, which further proves the accuracy of the calculation in this section.

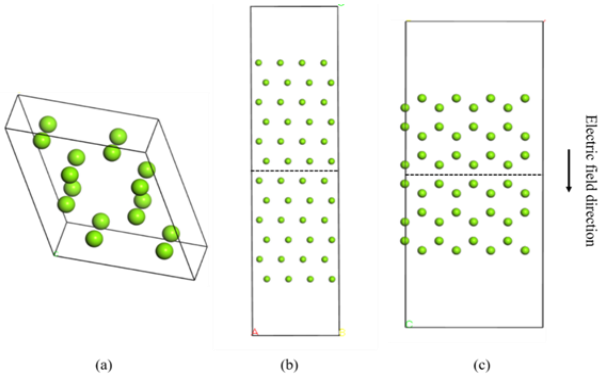

Figure 2 Calculation model: (a) Mg crystal model, (b) Mg basal plane model, (c) Mg prismatic surface model)

Table 3 Lattice parameters of Mg

	Mg	
	a/nm	c/nm
Cal	0.3209	0.5210
Ref[13]	0.3209	0.5211

3 Results and Discussion

3.1 Morphology of rolled pieces

Figure 3 shows the sample morphology of AZ91D magnesium alloy rolled under different rolling conditions. It can see from the surface morphology of AZ91D magnesium alloy after rolling that the surface crack and edge crack of AZ91D magnesium alloy obviously improve under electric pulse rolling. Under the ordinary cold rolling condition, large cracks and small edge cracks appeared on the surface of the sample from the boundary to the middle position. Under the condition of electric pulse cold rolling, only a few edge cracks appear on the surface of AZ91D magnesium alloy samples, which significantly improves compared with that under the condition of ordinary cold rolling. Under ordinary hot rolling condition, fine boundary cracks appear on the surface of AZ91D magnesium alloy samples, and the surface morphology is similar to that under electric pulse cold rolling condition. Under the condition of electric pulse hot rolling, there is no obvious crack on the surface of AZ91D magnesium alloy sample, and the edge crack obviously improves. The results indicate that electric pulse rolling can obviously improve the surface crack of AZ91D magnesium alloy.

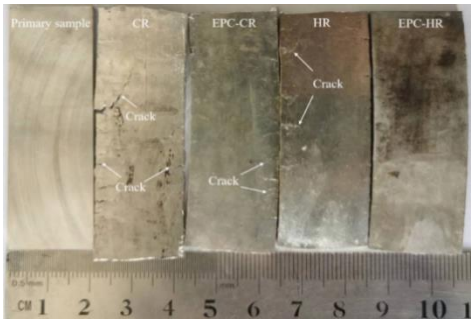

Figure 3 Morphology of AZ91D magnesium alloy samples rolled under different rolling conditions

3.2 Effect of electric pulse rolling on texture of AZ91D magnesium alloy

Figure 4 shows the EBSD image and pole diagram of AZ91D magnesium alloy after rolling with different process parameters. Figure 4a and 4b show the EBSD images of the samples after ordinary cold rolling and electric pulse cold rolling, respectively. It can clearly see from the figure the texture strength of the samples after electric pulse cold rolling in the direction of 0002 and 1010 decreases significantly, from 18.11 and 6.51 to 15.89 and 6.27, respectively. Figure 4c and 4d show the EBSD images of the samples after ordinary hot rolling and electric pulse hot rolling, respectively. After electric pulse applies to the hot rolled samples, the texture strengths in both directions of 0002 and 1010 also decrease, from 9.4 and 3.2 to 5.03 and 1.63.

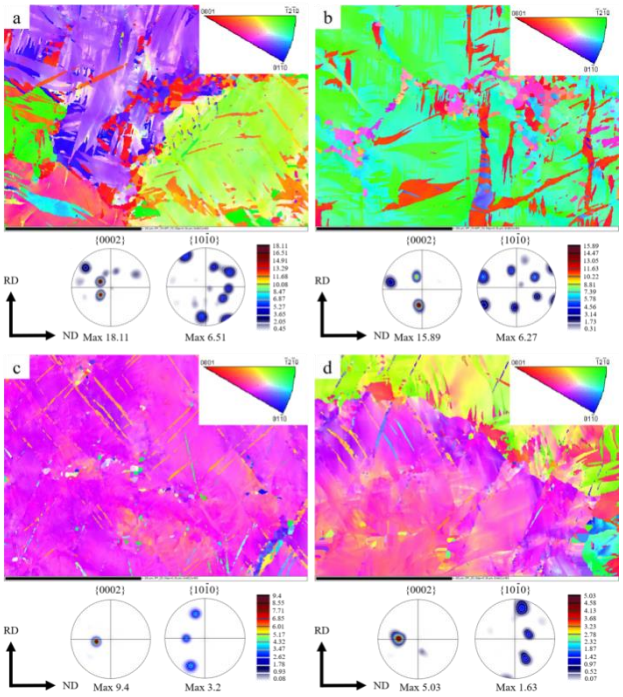

Figure 4 EBSD image of AZ91D magnesium alloy after rolling with different process parameters: (a) ordinary cold rolling, (b) electric pulse cold rolling, (c) ordinary hot rolling, d electric pulse hot rolling)

3.3 Effect of electric pulse rolling on twinning of AZ91D magnesium alloy

Figure 5 shows EBSD images of labeled twin grain boundaries of AZ91D magnesium alloy after rolling with different process parameters. The red line represents {1012} stretched twin boundary, the blue line represents {1011} compressed twin boundary, and the green line represents {1012}-{1011} secondary twin boundary. Figure 5a and 5b show the samples after ordinary cold rolling and electric pulse cold rolling respectively, while Figure 5c and 6d show the samples after ordinary hot rolling and electric pulse hot rolling respectively. EBSD images of labeled twinned grain boundaries of cold-rolled and hot-rolled samples show the content of twinned grain in hot-rolled samples is significantly lower than that in cold-rolled samples. This is because the increase of temperature reduces the Critical Resolved Shear Stress (CRSS) of magnesium alloy non-basal slip system. More slip systems involve in the plastic deformation of magnesium alloy. However, in the cold rolling process at room temperature, only two basal slip systems share in the plastic deformation, which is not enough to completely coordinate the grain deformation, so twin deformation will occur. Therefore, the content of twins in cold rolled samples is significantly higher than that in hot rolled samples. EBSD images of labeled twin grain boundaries of the samples after ordinary rolling and electric pulse rolling show the twin content of the samples with electric pulse rolling is slightly lower than that of the samples without electric pulse rolling at the same temperature. For cold rolled samples, the twin content increases from 8.64% to 15.1% after electric pulse rolling. For the hot rolled sample, the twinning content of the sample increased from 1.66% to 3.24% after electric pulse application. The twin grain boundaries contents of the samples rolled with electric pulse rolling are higher but not lower than those of the samples rolled without electric pulse.

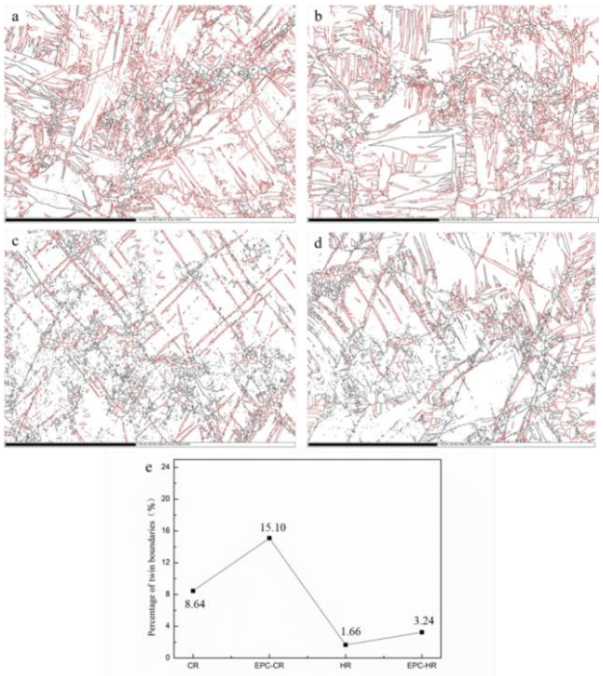

Figure 5 EBSD images of labeled twin grain boundaries of AZ91D magnesium alloy under different rolling parameters:(a) the ordinary cold rolled sample, (b) the electric pulse cold rolled sample, (c) the ordinary hot rolled sample, (d) the electric pulse hot rolled sample

3.4 Effect of electric pulse rolling on orientation difference distribution of AZ91D magnesium alloy

Figure 6 shows the distribution of grain boundary Angle orientation difference of AZ91D magnesium alloy after rolling with different process parameters. Figure 6a and 6b show the distribution of grain boundary Angle orientation difference after ordinary cold rolling and electric pulse cold rolling, respectively. Figure 6c and 6d show the distribution of grain boundary Angle orientation difference after ordinary hot rolling and electric pulse hot rolling, respectively. It can see from the figure that all the rolled samples under the four different processes have a peak at ~86°, and the peak of ~86° in the sample after electric pulse application is significantly higher than that in the sample without electric pulse application, showing the introduction of pulse current promotes the generation of tensile twins in AZ91D magnesium alloy, which is consistent with EBSD image analysis of twin grain boundaries. The peak of ~40° appeared in the hot rolled sample, which obviously reduced after the application of electric pulse. In addition, the small Angle grain boundary content of < 5° decreased after the application of electric pulse. For the cold rolled sample, the small Angle grain boundary content of < 5° decreased from 71% to 63% after the application of pulse current. For the hot rolled sample, the grain boundary content of small Angle < 5° decreased from 79% to 77% after pulse current application.

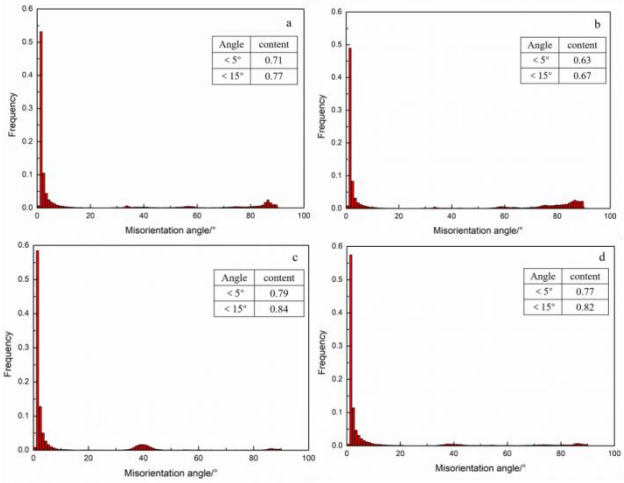

Figure 6 Distribution of grain boundary angular orientation difference of AZ91D magnesium alloy after rolling with different process parameters:(a) the ordinary cold rolled sample, (b) the electric pulse cold rolled sample, (c) the ordinary hot rolled sample, (d) the electric pulse hot rolled sample

3.5 Effect of electric pulse rolling on microhardness of AZ91D magnesium alloy

Figure 7 shows the microhardness of each phase of AZ91D magnesium alloy after rolling with different process parameters. As can be seen from the figure, the microhardness of α-Mg matrix of the cold-rolled sample decreases by 15.7% from 61.1HV to 51.5HV after pulse

current application, which is 8.1% lower than that of the original unrolled AZ91D magnesium alloy sample of 56.1HV. The microhardness of α-Mg matrix decreased from 60.5HV to 51.5HV by 14.8%, which was 8.1% lower than that of original unrolled AZ91D magnesium alloy sample (56.1HV).

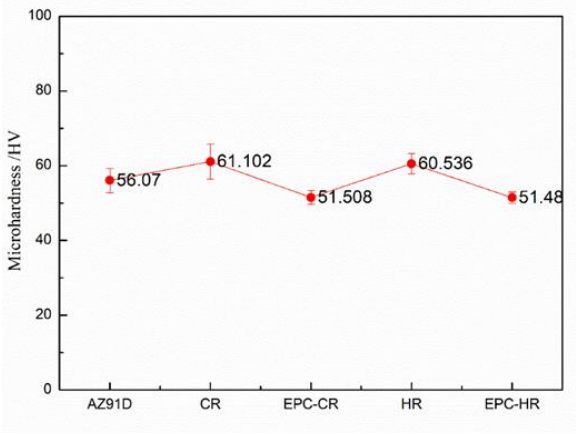

Figure 7 Microhardness of AZ91D magnesium alloy phases after rolling with different process parameters

3.6 Effect of electric pulse rolling on tensile properties of AZ91D magnesium alloy

Figure 8 shows the average tensile strength and average elongation of AZ91D magnesium alloy after rolling with different process parameters. As can see from the figure, the tensile strength of the rolled AZ91D magnesium alloy sample is significantly higher than that of the unrolled original AZ91D magnesium alloy sample. The elongation of the ordinary cold rolled AZ91D magnesium alloy sample is lo``wer than that of the unrolled original AZ91D magnesium alloy sample. For the cold-rolled samples, the tensile strength and elongation increased from 106MPa and 1.5% to 127MPa and 3.5%, respectively. For the hot rolled samples, the tensile strength and elongation increased from 137MPa and 3.4% to 169MPa and 4.7%.

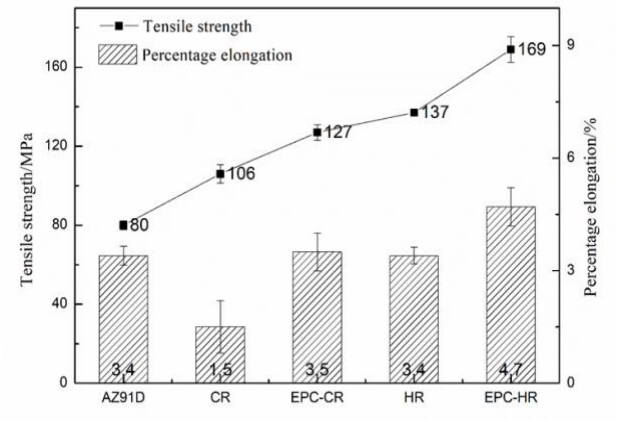

Figure 8 Tensile properties of AZ91D magnesium alloy after rolling with different process parameters

Figure 9 shows SEM images of fracture of AZ91D magnesium alloy rolled with different process parameters. Figure 8a shows the fracture morphology of unrolled original AZ91D magnesium alloy sample. Figure 8b and 8c show the fracture morphology of AZ91D magnesium alloy after ordinary cold rolling and electric pulse cold rolling respectively. Figure 8d and 8e show the fracture morphology of AZ91D magnesium alloy after ordinary hot rolling and electric pulse hot rolling respectively. It can see from the figure that, There are a lot of cracks and dissociation steps in the fracture of unrolled AZ91D magnesium alloy samples, and there is no dimple, so AZ91D magnesium alloy mainly presents brittle fracture. The fracture morphology of AZ91D magnesium alloy after common cold rolling is similar to that of original AZ91D magnesium alloy, both of which have many cracks and dissociation steps. The fracture of AZ91D magnesium alloy after electric pulse cold rolling has a dimple also cracks and dissociation steps. Similar to cold rolling, there are many cracks and dissociation steps in the fracture of AZ91D magnesium alloy after ordinary hot rolling, and there are almost no dimples. However, there are cracks and dissociation steps in the fracture of AZ91D magnesium alloy after electric pulse hot rolling, with many dimples, and the fracture types are mainly brittle fracture and ductile fracture.

Figure 10 shows the fixed-point EDS images of the fracture of AZ91D magnesium alloy rolled with different process parameters. EDS spectra analyzed at the crack and dissociation step at point 1 and point 2, respectively, and at the dimple at point 3. According to the results of energy spectrum analysis, the crack and dissociation step are the mixed phase of β-Mg17Al12 phase and α-Mg phase, while the dimple is α-Mg matrix phase. It can see the α-Mg matrix changes from the brittle phase to the ductile phase after pulse current application, which improves the elongation of AZ91D magnesium alloy.

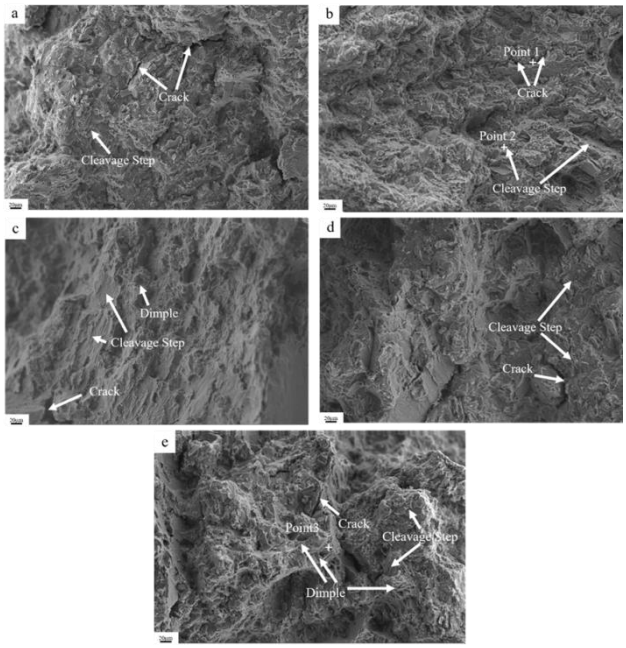

Figure 9 SEM images of fracture of AZ91D magnesium alloy rolled with different process parameters: (a) the original unrolled sample, (b) the ordinary cold rolled sample, (c) the electric pulse cold rolled sample,(d) the ordinary hot rolled sample, (e) the electric pulse hot

rolled sample

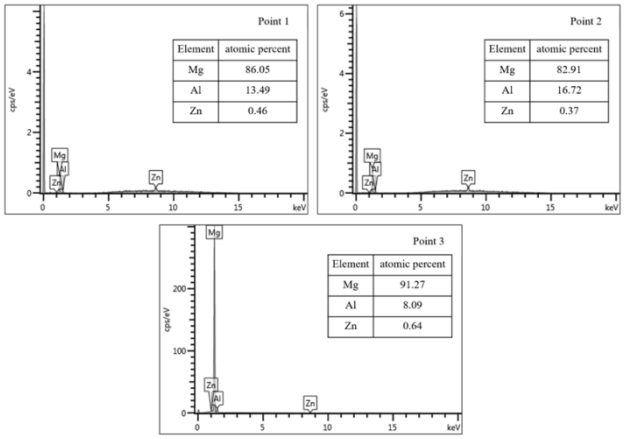

Figure 10 Image of EDS energy spectrum analysis

3.7 First principles computational analysis

3.7.1 Mechanical properties

The effect of electric field on mechanical properties of Mg studied by first principles calculation method. The elastic constant Cij of Mg before and after electric field application calculated, and the anisotropy characteristics of Mg under applied electric field further studied. The bulk modulus B, shear modulus G, Young's modulus E and Poisson's ratio V were mainly calculated. The calculation results show in Table 4. The bulk modulus B refers to the ability of a material to resist compression deformation under applied external stress. For solid materials, within their elastic limits, the larger the volume modulus B is, the stronger the compression deformation resistance is. As can see from Table 4, after the electric field applies, the volume modulus B of Mg increases, and it becomes difficult to compress. Shear modulus G refers to the ability of a material to resist shear strain under shear stress. When the value of shear modulus G of a material increases, its stiffness increases. It can see from Table 4 that after the application of electric field, Mg's shear modulus G decreases, and its stiffness becomes weaker. Young's modulus E is within the elastic limit, the material is the ratio of stress and the stress caused by the strain, with the same shear modulus, the higher the value of young's modulus E, the stronger the stiffness of the material. From the table 4 shows that after applying an electric field, the value of young's modulus E of Mg decreased, its stiffness weak, are consistent with the shear modulus. Poisson's ratio v refers to when the material to be pull (pressure) stress, transverse and axial strain ratio, the greater the material poisson's ratio value, its plasticity, the better [14]. From table 4 shows that after applying an electric field, poisson's ratio of Mg values increase, its plasticity is also improved, with the former analysis of the tensile fracture surface consistent. The elastic modulus ratio B/G can be used to evaluate the brittleness and plasticity of the material. When the value of B/G is greater than 1.75, the material exhibits ductility, and the larger the value, the better the plasticity of the material, and otherwise, the material exhibits brittleness. As can see from Table 4, the B/G value of Mg increased significantly by 1.75 after the electric field applied. Its plasticity improve. Hardness H is an important index for evaluating material properties, which refers to the ability of the material to resist hard objects pressing into the surface locally. It can see from Table 4 the hardness of Mg decreases significantly after the electric field applies, which is consistent with the experimental results above and further proves the accuracy of the calculation.

Table 4 Calculation results of mechanical properties of Mg before and after electric field application

	B/GPa	G/GPa	E/GPa	v	A	B/G	H/GPa
Mg	36.38	16.41	42.78	0.3	0.3	2.21	2.14
EP-Mg	52.60	14.47	39.77	0.37	0.45	3.64	1.21

3.7.2 Generalized layered fault energy

The generalized layered fault energy refers to the energy difference between the crystal cells per unit area on a certain slip surface before and after the formation of layered fault. The formula for calculating the generalized layered fault energy γ is:

$$\gamma = \frac{E-E_0}{A} \quad (3\text{-}1)$$

Where, E0 is the total energy of the intact crystal, E is the total energy of the crystal after lamination, and A is the lamination area.

The total energy of the complete crystal structure of Mg system obtained by structural relaxation of the thin plate model of Mg base plane and prismatic plane. The total energy of the layered fault structure calculated by structural relaxation of 0.1b for each slip plane movement. The calculated data were put into Equation 3-1 to obtain the generalized layered fault energy. It generally believes the size of the unstable fault energy γus indicates the difficulty of the slip system along the slip plane. The larger the value of γus, the more difficult the slip is to start, and the worse the plastic forming ability of the material is. The generalized layered fault energy of Mg's base plane and its prismatic plane before and after applying electric field calculates by the above method, and the calculation results are shown in figure 11.

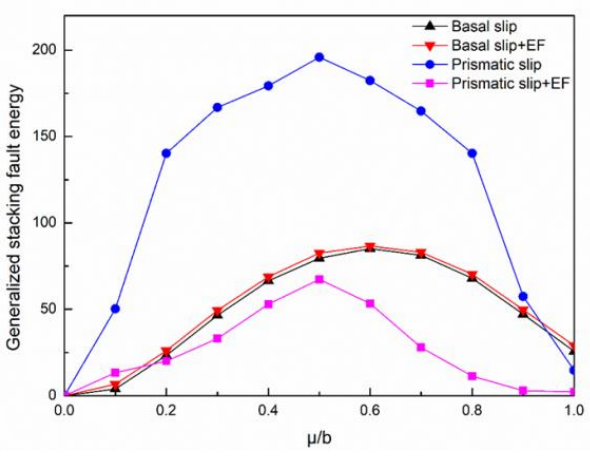

Figure 11 Generalized layered fault energy curves of

Mg base plane and prism plane before and after electric field application

As can see from figure 10, when no electric field applies, the generalized layered fault energy of Mg prism surface is significantly larger than that of its base surface. The unstable layered fault energy of Mg prism surface is γus=196mJ/m^2. The unstable layered fault energy of Mg base surface is γus=80mJ/m^2, showing that under ordinary conditions, Mg prism slip system is more difficult to start than the base slip system. This is also confirmed by the deformation theory of Mg. After the electric field is applied, the generalized layered fault energy of Mg base surface does not change much, and its unstable layered fault energy γus remains about 80mJ/m^2. However, after the electric field applies, the generalized layered fault energy of Mg prism surface decreases significantly, and its unstable layered fault energy γus decreases from 196mJ/m^2 to 67mJ/m^2. The results show the Mg prismatic slip system is easier to start after the electric field is applied, and thus the plastic forming ability of Mg is improved.

Poty et al. [15] studied the dislocation mobility of Zr and Ti with dense hexagonal structure by measuring the ratio of γuS (basal) layer fault energy to Prism (Prism) layer fault energy. It is reasonable to use the ratio of basal and Prism unstable layer fault energy γus as the criterion of Mg anisotropy. For table 5 Mg base level before and after applying an electric field and layer on the surface of the prism is not stable can gamma us wrong and its ratio. From the data in table 5 shows that after applying an electric field model of Mg base unstable layer can wrong with prismatic surface instability fault energy ratio closer to 1. The above experimental results show the introduction of the electric field can reduce the strength of the base surface texture, therefore. The introduction of electric field improves the anisotropy of Mg, which leads to the reduction of basal texture, and then makes Mg have higher formability.

Table 5 Unstable layered fault energies γus and their ratios at Mg base and prismatic surfaces before and after electric field application

	γ_{us}(basal)	γ_{us}(prism)	γ_{us}(basal)/γ_{us}(prism)
Mg	85.12	182.41	0.46
EP-Mg	86.66	67.36	1.28

4 Conclusion

(1) Pulse current applied in the rolling process of AZ91D magnesium alloy can effectively improve the edge crack of the sample, optimize the texture of AZ91D magnesium alloy and reduce its texture strength. In addition, pulse current can promote the formation of tensile twins and the transition from small Angle grain boundaries to large Angle grain boundaries, which improves the plastic forming ability of AZ91D magnesium alloy.

(2) When pulse current is applied during AZ91D magnesium alloy rolling, the microhardness of α-Mg matrix decreases by about 15% compared with ordinary rolling. The tensile strength and elongation increased from 137MPa and 3.4% to 169MPa and 4.7%, respectively. In addition, dimples appear in the AZ91D magnesium alloy samples after electric pulse rolling, and dimples are concentrated in the α-Mg matrix, showing the introduction of pulse current can promote the transition from brittle to ductile fracture of AZ91D magnesium alloy.

(3) After the application of electric field, the stiffness of Mg decreases, the Poisson's ratio of Mg increases, and the B/G value increases significantly by 1.75, which improves its plasticity.

(4) When the electric field is applied, the fault energy of Mg's base surface does not change much. But the fault energy of Mg's prismatic surface decreases obviously, showing the external electric field mainly affects Mg's prismatic surface slip, which makes Mg's prismatic surface slip easier to start, and thus improves the plastic forming ability of Mg.

Acknowledgments

The work was supported by the National Natural Science Foundation of China [grant number 52061002].

Conflict of Interest Statement

All authors disclosed no relevant relationships.

References

[1] X. Hao, W.X. Hao, G.H. Geng, et al.. Effects of High-Density Pulse Currents on the Solidification Structures of Cu-SiCp/AZ91D Composites Advances in Materials Science and Engineering. 2019(1): 1-6.

[2] Y. Xu, C. Chen, X.X. Zhang, et al.. Dynamic recrystallization kinetics and microstructure evolution of an AZ91D magnesium alloy during hot compression Materials Characterization. 2018(145): 39-52.

[3] W.J. Li, K.K. Deng, X. Zhang, et al.. Microstructures, tensile properties and work hardening behavior of SiCp/Mg-Zn-Ca composites Journal of Alloys and Compounds. 2017(695): 2215-2223.

[4] K. Edalati, R. Uehiro, Y. Ikeda, et al.. Design and synthesis of a magnesium alloy for room temperature hydrogen storage Acta Materialia. 2018(149): 88.

[5] J. Kuang, X.H. Li, R.K. Zhang, et al.. Enhanced rollability of Mg-3Al-1Zn alloy by pulsed electric current: a comparative study Materials & Design. 2016(100): 204.

[6] J. Kuang, X.H. Li, R.K. Zhang, et al.. Enhanced rollability of Mg-3Al-1Zn alloy by pulsed electric current: a comparative study Materials & Design. 2016(100): 204.

[7] P.J. Zhao, Z.H. Chen, C.F. Dong. Damage and Failure Analysis of AZ31 Alloy Sheet in Warm Stamping Processes Journal of Materials Engineering and Performance. 2016,25(7):2702.

[8] N. Stanford, R.K.W. Marceau, M.R. Barnett. The effect of high yttrium solute concentration on the twinning behaviour of magnesium alloys Acta Materialia. 2015(82):447.

[9] I. Indhiarto, T. Shimizu, M. Yang. Effect of Peak Current

Density on Tensile Properties of AZ31B Magnesium Alloy Materials. 2021, 14(6):5.

[10] K. Liu, X.H. Dong, H.Y. Xie, et al.. Influence of pulsed current on deformation mechanism of AZ31B sheets during tension Journal of Alloys and Compounds. 2016(676): 106.

[11] Vitek, V. Intrinsic stacking faults in body-centred cubic crystals. Philosophical Magazine,1968, 18(154): 773-786.

[12] M. Yuasa, M. Hayashi, M. Mabuch, et al.. Improved plastic anisotropy of Mg-Zn-Ca alloys exhibiting high-stretch formability: A first-principles study Acta Materialia. 2014(65): 207.

[13] Guangyin Yuan, Yangshan Sun, Wenjiang Ding. Effects of Sb addition on the microstructure and mechanical properties of az91 magnesium alloy. Scripta Materialia, 2000, 43(11): 1009-1013.

[14] S. Sandlobes, M. Friak, S. Zaefferer, et al.. The relation between ductility and stacking fault energies in Mg and Mg-Y alloys Acta Materialia. 2012, 60(6-7): 3011.

[15] Zhang J, Mao C, Long C G, et al.. Phase stability, elastic properties and electronic structures of Mg-Y intermetallics from first-principles calculations[J]. Journal of Magnesium & Alloys, 2015, 3(2): 127-133.

[16] S.F. Matar, R. Pottgen, B. Chevalier. Electronic and magnetic structures and bonding properties of Ce_2T_2X (=nd element; X = Mg, Cd, Pb or Sn) intermetallics from first principles Intermetallics. 2014(51): 18.

Viser Technology Pte. Ltd.
Research and Application of Materials Science
DOI: 10.33142/rams.v4i2.8467

Research Article Open Access

$Co_{47.5}Fe_{28.\cdot 5}Ni_{19}Si_{3.3}Al_{1.7}$ High-entropy Skeletons Fabricated by Selective Laser Melting and Properties tuned by pressure infiltration of Al

Yaqi WU[1], Yongsen CAI[1], Jinpeng HAO[1], Guihong GENG[2], Yong ZHANG[1*]

1 State Key Laboratory for Advanced Metals and Materials, University of Science and Technology Beijing, Beijing 100083, China
2 School of Materials Science and Engineering, North Minzu University, Yinchuan 750030, China

***Corresponding Author:** Yong Zhang, E-mail: drzhangy@ustb.edu.cn*

Abstract:
High saturation magnetization and low coercivity are required for soft magnetic materials. This study investigated the $Co_{47.5}Fe_{28.5}Ni_19Si_{3.3}Al_{1.7}$ high-entropy soft magnetic skeleton was prepared by selective laser melting. Then Al was pressure infiltrated into skeletons to obtain a dense composite material. The high-entropy composite materials possessed favorable compressive ductility and moderate soft magnetic properties. The high-entropy composite materials were obtained with Ms being 97.1 emu/g, 79.8 emu/g, 33 emu/g and possessing 19 Oe, 15.8Oe and 17Oe of Hc, respectively. However, the magnetostriction coefficient remains low level, about 5ppm. These reported properties are attributed to the special structure of the material studied in present experiment. Nevertheless, a novel strategy of structural designing was proposed in this paper.

***Keywords:** High entropy alloy，Composite material，Selective laser melting，gas pressure infiltration，Soft Magnetic Properties*

1 Introduction

High entropy alloys (HEAs) have attracted much attention, due to their excellent mechanical and physical properties [1-6]. The appearance of HEAs has widened the composition design space, bringing more possibilities for development of materials. Researchers have studied HEAs not only as structural materials but also as functional materials with excellent properties or the ability to serve under extreme conditions that conventional alloys cannot. With the rapid development of society, information and industrial society constantly put forward new requirements for excellent soft magnetic functional materials. Electrical and electronic equipment uses soft magnetic materials, which are easily magnetized and demagnetized [7-8]. The preparation process for silicon steel is complex and has low resistivity. Amorphous and nano soft magnetic alloys have annealed brittleness and are limited by size. Therefore, it is of great significance to develop a new kind of soft magnetic material to break through the limitations of previous materials.

Selective laser melting technology has many advantages over traditional smelting processes in terms of solidification process, thermodynamic process, microstructure, and so forth, resulting in many unique properties [9-11]. Therefore, combining it with SLM technology can produce traditional alloys and properties, such as saturation magnetic induction, coercivity, strength and plasticity, that cannot be achieved by traditional processes [12-14]. Studies about the magnetic properties of AlxCrCuFeNi2 ($0 < x < 1.5$) HEAs fabricated by laser metal deposition (LMD) [15] were founded that the FCC/L12 regions with low Al contents were weakly ferromagnetic. However, the Al-rich BCC/B2 regions were relatively soft with low coercivity, but being ferromagnetic with high saturation magnetization. When x = 1.3, the saturation magnetization and coercivity reached the maximum values, illustrating that the magnetic properties in this HEAs system could be adjusted by a paramagnetic element. In another investigation [16], the magnetic properties of AlCoxCr1-xFeNi ($0<x<1$) HEAs were researched. The results suggested that the saturation magnetization monotonically increased 6 times from 18.48 emu/g of AlCrFeNi (x=0) to 117.8 emu/g of AlCoFeNi (x=1), while the change in coercivity was non-monotonic, increasing by 7 times from AlCrFeNi (x = 0) to AlCo0.4Cr0.6FeNi (x=0.4), and then decreasing by 14 times from AlCo0.4$Cr_{0.6}$FeNi (x=0.4) to AlCoFeNi (x=1). The magnetic phase transition temperature for these HEAs showed a monotonic increasing trend with the increase of the Co content, and between x = 0.6 to x = 0.8, a secondary phase transition occurred in the composition range.

In this work, the structure of high-entropy skeleton

Received on November 14, 2022; Accepted on December 22, 2022

was designed and prepared by selective laser melting (SLM), and high-entropy composite materials were prepared by pressure infiltration process, so as to improve the mechanical properties of the skeleton structure.

2 Materials and methods

2.1 Alloys Preparation

316L stainless steel (100*100*20mm^3) was used for the substrate in the SLM technology forming process. Gas atomization and high-purity $Co_{47.5}Fe_{28.5}Ni_{19}Si_{3.3}Al_{1.7}$ HEA powders was used for SLM and its composition has been listed in Table 1. The powder particle size range is about 15-53 um which microstructure was shown in figure 1. Here, three types skeleton structures were designed for the following work of gas pressure infiltration. The skeleton models firstly were created by the SolidWorks software. As shown in the figure 2, the total size of the model is a square with 10*10*10mm3 size, but possessing different square-pore size and they are 0.6 mm, 0.7 mm, 0.8 mm, respectively. All skeleton samples were prepared by AFS-M120 SLM equipment produced by Longyuan AFS Co., Ltd.

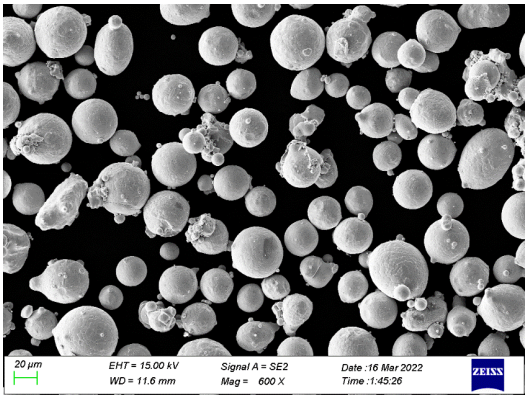

Figure 1 Microstructure of $Co_{47.5}Fe_{28.5}Ni_{19}Si_{3.3}Al_{1.7}$ powders

Table 1 Compositions of the $Co_{47.5}Fe_{28.5}Ni_{19}Si_{3.3}Al_{1.7}$ HEA powders

Elements	Co	Fe	Ni	Si	Al
Atomic ratio (at. %)	47.5	28.5	19.0	3.3	1.7

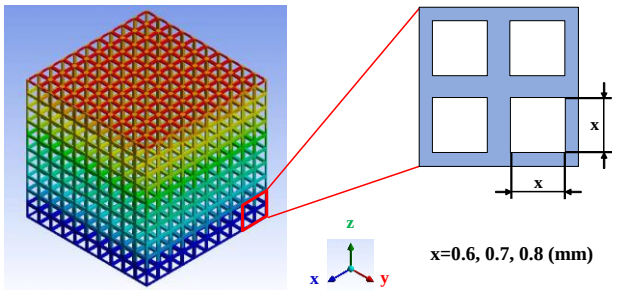

Figure 2 Schematic diagram of the porous structure of three types of high-entropy seleton with different square-pore sizes

Subsequently, pressure infiltration was carried out under high purity Ar atmosphere. Put the pure Al and $Co_{47.5}Fe_{28.5}Ni_{19}Si_{3.3}Al_{1.7}$ HEA skeleton into the pressure infiltration equipment, heating up the equipment to 800 degrees Celsius and keeping warm for 0.5 hours. After the Al melted, applied a pressure of 1 MPa to pressed Al into the high-entropy skeletons, followed by stopping heating and pressurizing when it was completed, then cooled down with the furnace.

2.2 Structural Characterization and Performance Experiments

A Bruker D8 Smart Lab X-ray diffractometer was utilized to determine the crystal structure, with Cu-Kα radiation ranging from 20° - 90°. The scanning rapid is 10°/min. The microstructure characterization and electron backscatter diffraction were measured using scanning-electron microscopy (SEM) with Zeiss Supera55 operated at 20 keV, along with energy-dispersive spectrometry (EDS). Compressive simples were a cylinder with φ3 × 6 mm cut by electro-discharge machining and compressive tests at strain rate of 5×10-3s-1 and 5×10-4s-1 for high-entropy skeleton and high-entropy composites, using CMT Model 4305 Universal Electronic Tester at room temperature respectively. The soft magnetic properties of samples with 3mm×2mm×2mm sizes were measured by vibrating sample magnetometer (VSM) under a magnetic field of ±1T at room temperature. The magnetostriction coefficient was obtained by the resistance strain gauge method.

3 Results and discussion

3.1 Phase formation and microstructure

We investigated the microstructure, compressive properties and soft magnetic properties of Al-$Co_{47.5}Fe_{28.5}Ni_{19}Si_{3.3}Al_{1.7}$ high-entropy composites structural material. Figure 3 is the macrostructure of the $Co_{47.5}Fe_{28.5}Ni_{19}Si_{3.3}Al_{1.7}$ high-entropy skeleton prepar ed by SLM.

The XRD pattern of high-entropy skeleton and high-entropy composites materials were shown in the figure 4(a) and figure 4(b). It is clearly shown that the main phase, a single face centered cubic (FCC) crystal of the skeleton, was identified. While several small peaks of compound phases appeared after pressure infiltration of aluminum. The X-ray diffraction analysis indicates that the porous material with high entropy only has one FCC phase, because the three phases of Fe, Co, and Ni dissolve into one solid solution, and trace amounts of Al and Si do not affect the overall FCC solid solution structure, and a single FCC solid solution performs.

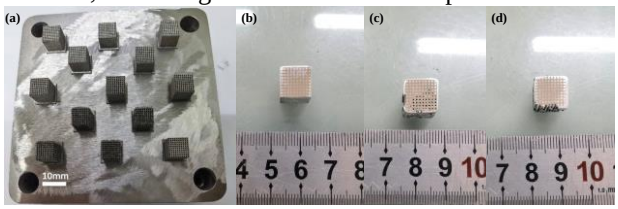

Figure 3 Macrostructure images of high-entropy skeletons prepared by SLM. (a) is high-entropy skeletons;(b)-(d)are high-entropy composite materials

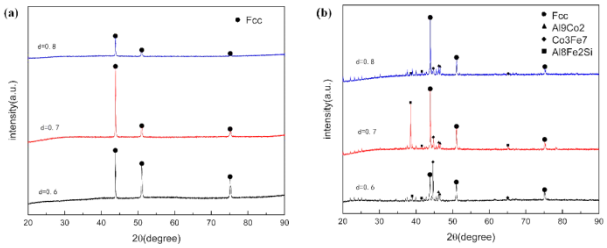

Figure 4 (a)X-ray diffraction patterns of $Co_{47.5}Fe_{28.5}Ni_{19}Si_{3.3}Al_{1.7}$ HEAs pores prepared by SLM with different side lengths and sizes of skeleton structures. (b)X-ray diffraction patterns of $Co_{47.5}Fe_{28.5}Ni_{19}Si_{3.3}Al_{1.7}$ high-entropy composites prepared by air pressure infiltration process

SEM images of high-entropy skeletons are presented in figure 5(1-a)-5(1-f), which exhibit smooth surface morphologies with the square shape of 0.6mm, 0.7mm and 0.8mm respectively. The cleary molten pool on the cross-section presents a classic scaly which are observed from figure 5(1-b), (1-d), (1-f). EBSD mapping as displaying in the figure 5(2), demonstrates that the high-entropy skeleton structure is a polycrystalline structure with the grain size between tens and two hundred microns. In areas A and B away from the boundary of the square-pores, the grains are relatively large. Moreover, in the central region A of the high-entropy skeleton, the grain size is relatively large, around 200 um. And the grain size is about 50 um in the suspension region B It can be seen that with the increasing of the square-pore size, the grain size tends to be uniform gradually. Figure 6 (2). EDS mapping illustrated that the five elements of Fe, Co, Ni, Al and Si are evenly distributed without element segregation in the high-entropy composite materials. The same as the results of the above SEM and XRD analysis.

(1)

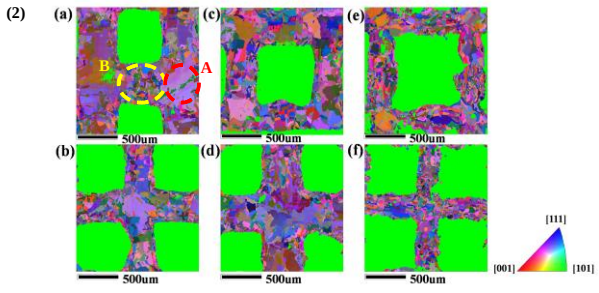

Figure 5 (1):SEM image of $Co_{47.5}Fe_{28.5}Ni_{19}Si_{3.3}Al_{1.7}$ high-entropy skeleton with different square-pore sizes(a)(b) the side length of the square-pore is 0.6 mm; (c)(d) the side length of the square-pore is 0.7 mm; (e)(f) the side length of the square-pore is 0.8 mm. (2): EBSD mapping of high-entropy skeleton

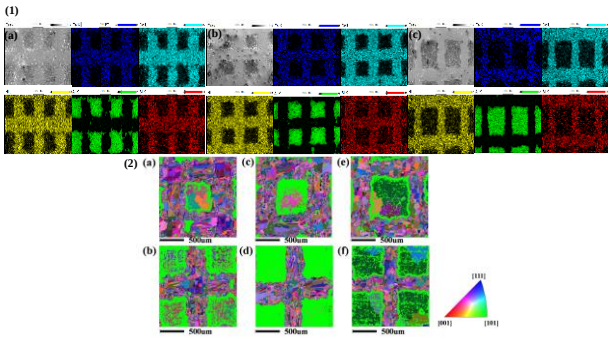

Figure 6 EDS and EBSD mapping of high-entropy composite with differen square size. (1-a)-(1-c) show the elemnts distrbution of high-entropy composites with different square-pores. (2) is the EBSD results of high-entropy composites materials

Owing to the high cooling rate (105 ～ 106 K/s) of the SLM process, the SLM Co47.5Fe28.5Ni19Si3.3Al1.7 alloy skeleton formed a non-equilibrium solidification organization, and this inhomogeneous tissue distribution can be attributed to the variation of local solidification conditions, which includes the temperature gradient (G) and solidification rate (R). The G/R value is determined by the undercooling of the composition at the solidification front of the melt pool, which in turn determines the morphology of the solidification structure. At the boundary of the molten pool, the heat of the melt can be conducted and dissipated through the SLM forming substrate. In the case of a single melt pool, the heat of the melt pool is first transferred to the solidified portion of the melt pool boundary [17-18].

The formation of large columnar grains in the middle of the melt pool, the heat-affected zone near the melt pool boundary is distributed with very fine equiaxed grains, and welding fusion zone structure is similar [19].

3.2 Mechanical properties

Compressive strain curves measured at room temperature (298K) are plotted in the figure 7. With the increasing of square-pores size, the strength of HEA-skeletons decreases. The slope decreases following the square-pore size increasing, which illustrates that as the square-pore size grows lager the Yong's modulus decreases. The same trends were observed from compressive strain curves of $Co_{47.5}Fe_{28.5}Ni_{19}Si_{3.3}Al_{1.7}$ high-entropy composite materials. Mechanical properties dates of high-entropy skeleton and composite materials were shown in Table 1. It can be observed that the strength increased and existed typical yield phenomenon obviously after infiltration of aluminum. In addition, HEA composites material performed excellent compressive ductility with loading increasing.

During the compression process, pores of different sizes reduce the load-bearing area, and also increase the loading stress initiating and promoting crack propagation, leading to premature failure of SLM-fabricated [20] With the pores being filled by Al, improved strength of the composite materials. On the other hand, the aluminum

element diffuses into the high-entropy alloy skeleton during the pressure infiltration process, forming intermetallic compounds of aluminum, which makes the dislocation movement hindered by grain boundaries and therefore increases the strength.

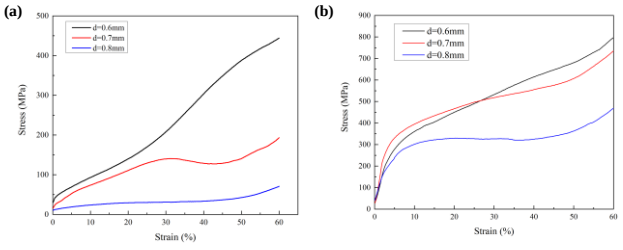

Figure 7 Compressive stress-strain curves of $Co_{47.5}Fe_{28.5}Ni_{19}Si_{3.3}Al_{1.7}$ HEAs skeleton and composites after infiltration at room temperature. (a): Properties of $Co_{47.5}Fe_{28.5}Ni_{19}Si_{3.3}Al_{1.7}$ HEAs skeleton. (b): Properties of $Co_{47.5}Fe_{28.5}Ni_{19}Si_{3.3}Al_{1.7}$ HEAs composites

3.3 Magnetic properties

The saturation magnetization and coercivity curves of HEA skeleton and composites can be obtained from figure 8(a) and (b). Figure 8(c) and (d) dispaly the Hc and Ms values bar of of high-entropy skeleton and composites respectively. According to figure 8, the saturation magnetizations of high-entropy skeletons fabricated by selective laser melting, are 146.2emu/g, 146.8emu/g and 151.3emu/g respectively. Experimental results were closed to that prepared by magnetic levitation melting we investigated in previous work [8].And the coercivity reaches14Oe, 9.9Oe, and 7.2Oe, respectively. After pressure infiltration of Al, values of Ms decreased markedly and Hc increased slightly. The Ms of the High-entropy composite materials are 97.1 emu/g, 79.8 emu/g, 33 emu/g and possess 19 Oe, 15.8Oe and 17Oe of Hc, respectively. The coercivity of the three composite materials is obviously larger than the limit value of soft magnetic materials (＜1000 A/m or 12.56 Oe).

Table 2 Compressive properties of $Co_{47.5}Fe_{28.5}Ni_{19}Si_{3.3}Al_{1.7}$ HEAs skeleton and composites after infiltration at room temperature.

d(mm)	$\sigma_{0.2}$(MPa)/ε_p(%) (HEA-skeleton)	$\sigma_{0.2}$(MPa)/ε_p(%) (HEA composites material)
0.6	45.6＞60%	240/＞60%
0.7	28.5＞60%	277.9/＞60%
0.8	13 ＞60%	198/＞60%

The saturation magnetization strength of soft magnetic materials is related to the constituent elements of the alloy [7, 21]. In the present experiment, the saturation magnetization strength of the high-entropy skeleton is comparable to that of the as-cast alloy, while the saturation magnetization strength decreases after pressure infiltration due to the fact that Al is a paramagnetic element with a magnetic moment close to 0, which leads to a decrease in saturation magnetization strength as the Al content increases [22]. The difference is that grain size and defects have a greater effect on the coercivity of the alloy.

It is known that the magnetic property of materials is dependent on the magnetic domains, in which the internal stress induced by crystalline defects could block the movement of domain walls in an applied magnetic field, leading to in an increase in the coercivity Hc. The grain size of the alloy prepared by SLM is around 100um [8], which is comparable to the cast state and therefore the coercivity is closer. It indicates that defects become the main influencing factor for the similar grain size. In this work, square-pores structure with different sizes in the high-entropy skeleton can be regarded as a macroscopic defect that causes a major shielding effect on the motion of magnetic domains.

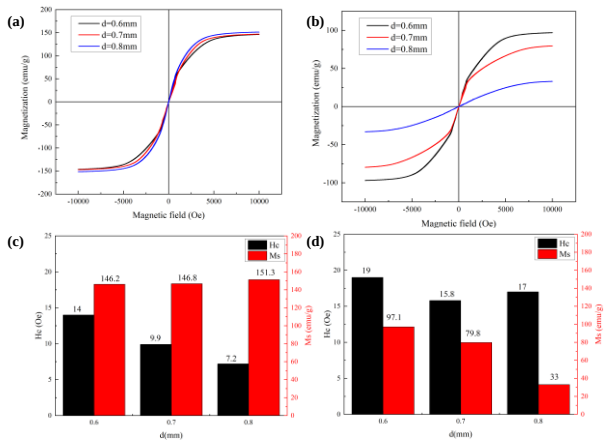

Figure 8 Room temperature hysteresis loops of $Co_{47.5}Fe_{28.5}Ni_{19}Si_{3.3}Al_{1.7}$ HEAs skeleton and composites

3.4 Magnetostriction characterization

Magnetostrictive coefficient curve are given in Figure 9 for $Co_{47.5}Fe_{28.5}Ni_{19}Si_{3.3}Al_{1.7}$ high-entropy skeleton and composite materials. It was found that the magnetostrictive coefficients of high-entropy skeleton and composite materials remained at the stable level, about 10 ppm and 5 ppm respectively. In comparison, the alloys $Co_{47.5}Fe_{28.5}Ni_{19}Si_{3.3}Al_{1.7}$ prepared by SLM in the present study possessed lower magnetostrictive performance than smelted by magnetic levitation [8].

Magnetostriction is the mechanical vibration of a material at the same frequency as the magnetic field under the action of an alternating magnetic field, i.e., the conversion of electromagnetic energy into mechanical energy. The magnetostriction coefficient is large, and the vibration generated by the conversion of mechanical energy is larger when the device is in operation, there will be noise generated. Hence, a lower magnetostriction coefficient will reduce the mechanical energy conversion and reduce the noise.

A number of researches indicated that prepared by SLM in the present study possessed better magnetostrictive performance than as-cast. For instance, Zhang et al. prepared bulk Fe-Ga alloys with 12 mm in diameter and 2 mm in thickness by casting and aging for 24 h. It was found that the λ//s (positive saturated magnetostriction) for the alloy with a thickness of 2 mm was 32 ppm and gradually increased with the thinning of

the alloy [23]. In addition, oriented bulk Fe-Ga rods prepared by directional solidification method, which showed large columnar crystals with ＜ 100 ＞ preferential orientation and a magnetostriction of 170 ppm [24]. However, in contrast to reported, the magnetostriction coefficients in present study were reduced. On the one hand, SLM process reduces the magnetostriction of the $Co_{47.5}Fe_{28.5}Ni_{19}Si_{3.3}Al_{1.7}$ skeleton and increases the blockage of the magnetic domain wall by irregular grains, which is not conducive to the uniform motion of the magnetic domain wall [25]. On the other hand, the special structure of the high-entropy skeleton impedes the movement of the magnetic domain walls, thus weakening the magnetostriction phenomenon of the alloy [26].

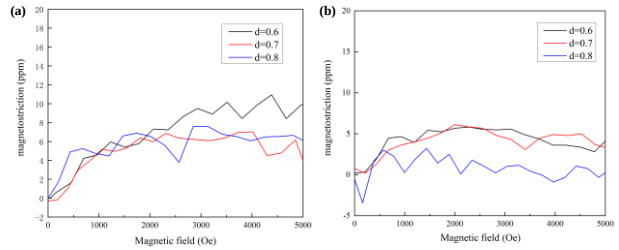

Figure 9 Magnetostrictive curves of $Co_{47.5}Fe_{28.5}Ni_{19}Si_{3.3}Al_{1.7}$ high-entropy skeletons and high-entropy composites materials.

4 Conclusions

This paper presents research on $Co_{47.5}Fe_{28.5}Ni_{19}Si_{3.3}Al_{1.7}$ high-entropy composites were prepared by selective laser melting and pressure infiltration. we developed three different high-entropy square-pore structures and composite materials. The following conclusions were drawn:

(1) $Co_{47.5}Fe_{28.5}Ni_{19}Si_{3.3}Al_{1.7}$ high-entropy skeleton were prepared by selective laser melting with a single FCC phase. And the compound phase of Al appears in the composite after Al pressure infiltration.

(2) Uneven grain size of the high entropy skeleton structure is the result of non-equilibrium solidification caused by the different cooling rates between the center and the boundary of the melt pool in the SLM process.

(3) The saturation magnetization strength decreases after pressure infiltration due to the fact that Al is a paramagnetic element with a magnetic moment close to 0, which leads to a decrease in saturation magnetization strength as the Al content increases. For the similar grain size, defects become the main influencing factor. In this work, square-pores structure with different sizes in the high-entropy skeleton can be regarded as a macroscopic defect that causes a major shielding effect on the motion of magnetic domains.

(4) The composites with different square-pore sizes exhibit favorable compressive plasticity with a degree of deformation above 60%. Strength of high-entropy composite materials was improved due to infiltration of Al into pore defects.

(5) The magnetostriction coefficient of high-entropy composite material is lower than that of high-entropy skeletons, but the magnetostriction coefficients of both are relatively low and more stable.

DECLARATIONS

Authors' contributions

Made substantial contributions to conception and design of the study and performed data analysis and interpretation: Yaqi Wu, Yongsen Cai, Jinpeng Hao; rovided technical, and material support: Yong Zhang.

Availability of data and materials

Not applicable.

Financial support and sponsorship

Y. Z. acknowledges supports from (1) National Natural Science Foundation of China (NSFC, Granted Nos. 51671020); (2) Guangdong Basic and Applied Basic Research Foundation (No.2019B1515120020); and (3) Creative Research Groups of China (No.51921001).

Conflicts of interest

All authors declared that there are no conflicts of interest.

References

[1] Zhang Y, Amorphous and High entropy alloys. China Science Publishing & Media Ltd; 2010(1):125-130.

[2] Beke D L, Erdélyi G. On the diffusion in High entropy alloys [J]. Materials Letters 2016(164): 111-113.

[3] Gao M C, Liaw P K, Yeh J W, et al.. High entropy alloys: Fundamentals and applications [J]. 2016(1), 210-221.

[4] Gao M C, Miracle D B, Maurice D, et al.. High-entropy functional materials. Journal of Materials Research 2018, 33(19): 3138-3155.

[5] Xue H Y, Jin S L, Wei R Z, et al.. A Brief Review of High-Entropy Films [J]. Journal of Materials Chemistry and Physics, 2017(1): 210.

[6] Yeh J W, Chen S K, Lin S J, et al.. Nanostructured High entropy alloys with Multiple Principal Elements: Novel Alloy Design Concepts and Outcomes. Advanced Engineering Materials 2004, 6(5): 299-303.

[7] Herzer G. Modern soft magnets: Amorphous and nanocrystalline materials. Acta Materialia 2013, 61(3): 718-734.

[8] Zhang Y, Zhang M, Li D Y, et al.. Metals Compositional Design of Soft Magnetic High Entropy Alloys by Minimizing Magnetostriction Coefficient in (Fe0.3Co0.5Ni0.2)100 − x(Al1/3Si2/3)x System [J]. 2019, 9(3):5-6.

[9] D. Herzog, V. Seyda, E. Wycisk, et al.. Additive manufacturing of metals [J]. Acta Mater, 2016(117): 371-392.

[10] S. Chen, Y. Tong, P. Liaw, Additive manufacturing of high-entropy alloys: A review [J]. Entropy, 2018, 20(12): 937.

[11] H. Dobbelstein, E.L. Gurevich, E.P. George, et al.. Laser metal deposition of compositionally graded TiZrNbTa

refractory high-entropy alloys using elemental powder blends [J]. Addit. Manuf, 2019(25):252-262.
[12] L C Huang, Y N Sun, A. Abdukadir, et al.. Microstructure and mechanical properties of AlxCoCrFeNi High entropy alloys deposited by laser melting [J]. Vaccum, 2021(183):109875.
[13] Wang S, Liu Y D, Qi B, et al.. Study on the forming process and performance of 316L large layer thickness by selective laser melting [J]. Applied Laser, 2017, 37(6):7.
[14] Wang Z K, Zheng Q G, Wang T, et al.. Coagulation tissue feature formation process of laser surface cladding layer [J]. Laser technology 2000(1):66-68.
[15] T. Borkar, B. Gwalani, D. Choudhuri, et al.. A combinatorial assessment of AlxCrCuFeNi2 (0 ＜ x ＜ 1.5) complex concentrated alloys: microstructure, microhardness, and magnetic properties [J]. Acta Mater,2016(6):63-76.
[16] T. Borkar, V. Chaudhary, B. Gwalani, et al.. A combinatorial approach for assessing the magnetic properties of high entropy alloys: role of Cr in AlCoxCr1-xFeNi (0＜x＜1.5) [J]. Adv. Eng. Mater, 2017, 19 (8):1700048.
[17] Carter L N, Withers P J, Martin C. The influence of the laser scan strategy on grain structure and cracking behaviour in SLM powder-bed fabricated nickel superalloy [J]. Journal of Alloys and Compounds, 2014(615):338-347.
[18] Y.Y. Chen, H. Yue, X.P. Wang. Microstructure, texture and tensile property as a function of scanning speed of Ti47Al2Cr2Nb alloy fabricated by selective electron beam melting [J]. Mater. Sci. Eng. A, 2018(713):195-205.
[19] S.J. Wolff, S. Lin, E.J. Faierson, et al.. A framework to link localized cooling and properties of directed energy deposition (DED)-processed Ti-6Al-4V [J]. Acta Mater. 2017(132): 106-17.
[20] L. Lan, W. Wang, Z. Cui, et al.. Anisotropy study of the microstructure and properties of AlCoCrFeNi2.1 eutectic high entropy alloy additively manufactured by selective laser melting[J]. J. Mater. Sci. Technol., 2022(129):229-239.
[21] Huang B, Yang Y, Wang A D, et al.. Saturated magnetization and glass forming ability of soft magnetic Fe-based metallic glasses [J]. Intermetallics 2017(84):74-81.
[22] Zhang Y, Zuo T T, Cheng Y Q, et al.. High entropy alloys with High Saturation Magnetization[J]. Electrical Resistivity, and Malleability. Scientific Reports 2013(3):1455.
[23] J.H. Li, X.X. Gao, X.M. Xiao, et al.. M.-C. Zhang, Magnetostriction of ＜100＞ oriented Fe-Ga rods with large diameter [J]. Rare Met, 2015, 34 (7):472-476.
[24] Y. Zhang, P. Sun, J. Gou, et al.. Depth-dependent decomposition and property of large magneto-striction Fe-Ga alloys [J]. Appl. Surf. Sci, 2021(569):151059.
[25] G.D. Liu, X.F. Dai, Z.H. Liu, et al.. Structure, magnetostriction, and magnetic properties of melt-spun Fe-Ga alloys [J]. J. Appl. Phys, 2016, 99 (9):093904.
[26] A.A. Emdadi, S.H. Nedjad, H.B. Ghavifekr. Effect of solidification texture on the magnetostrictive behavior of galfenol [J]. Metall. Mater. Trans. A, 2014, 45 (2): 906-910

Viser Technology Pte. Ltd.
Research and Application of Materials Science
DOI: 10.33142/rams.v4i2.8468

Research Article Open Access

Effects of Nickel on the Microstructure, Mechanical properties and Corrosion Resistance of $CoCrFeNi_xAl_{0.15}Ti_{0.1}$ High Entropy Alloy

Wu QI [1, 3], Yitian SU [1, 3], Xiao YANG [2*], Guannan ZHANG [2], Yi ZHAO[4], Ya ZHANG[5], Wenrui WANG[1, 3*]

1 School of Mechanical Engineering, University of Science and Technology Beijing, Beijing 100083, China
2 Key Laboratory of Cryogenics, Technical Institute of Physics and Chemistry, Chinese Academy of Sciences, Beijing 100190, China
3 Key Laboratory of Fluid Interaction with Material, Ministry of Education, Beijing 100083, China
4 Unit 92228, People's Liberation Army, Beijing 100072, PR China
5 Beijing Aerospace Petrochemical Technology & Equipment Engineering Corporation Limited, Beijing 100176, China

***Corresponding Author:** Xiao YANG, E-mail: yangxiao@mail.ipc.ac.cn; Wenrui WANG, E-mail: gmbitwrw@ustb.edu.cn*

Abstract:
The present work investigates the effect of Ni on the microstructure, mechanical properties, and corrosion resistance of $CoCrFeNi_xAl_{0.15}Ti_{0.1}$ high-entropy alloys. It was found that the appropriate addition of Ni element in the alloy is beneficial to reduce the average grain size of the alloy. The yield strength and tensile strength of the alloy under fine-grain strengthening have also been increased, while the ductility of the system in this study has not been significantly affected. In terms of corrosion resistance, $CoCrFeNi_xAl_{0.15}Ti_{0.1}$ high-entropy alloys form a dense passive film at open circuit potential, possessing good corrosion resistance. However, with the excessive addition of Ni content in the alloy, the pitting corrosion resistance of the alloy in the environment of chloride ions will decrease due to the relative decrease of the relative content of Cr element. This work also can provide guidances for the design and development of new precipitation-strengthened CoCrFeNi-based high-entropy alloys with excellent comprehensive properties.

Keywords: *High-entropy alloy, Microstructures, Mechanical properties, Corrosion resistance*

1 Introduction

In recent years, high-entropy alloys (HEAs) have become a hot research object in the field of metal materials for its excellent comprehensive properties [1-5]. Different from the design concept of traditional alloys with a single principal element, HEAs containing four or more elements designed in equal or near-equal proportions tend to form a multi-component disordered solid solution phase structure [6-7]. Due to excellent ductility at room temperature and low temperature, the most representative CoCrFeNi high-entropy alloy with FCC structure has been widely studied [8-9]. Additionally, the CoCrFeNi alloys can form a uniform, dense and stable high-entropy amorphous oxide passive film on the surface in an oxygen environment, which can lead to excellent corrosion resistance [10-12]. However, the low strength of FCC-structured CoCrFeNi high-entropy alloys limits the range of industrial applications.

In the past few years, many researches have been carried out on strengthening CoCrFeNi HEAs. In traditional structural alloys, such as superalloys, steels, aluminum alloys, etc., precipitation strengthening has been proven to be one of the effective ways to improve the strength of metal materials [13-15]. Due to the multi-component characteristics of CoCrFeNi-based HEA, there are many types of strengthening phases can be induced to precipitate. Common precipitation strengthening phases include Laves phase and L12-γ′ phase [16-18]. However, though the addition of common Nb, Hf, Ta and other large-sized atoms to form the precipitation of Laves phase can improve the mechanical properties of the alloy, it will also seriously reduce the toughness of the alloys [19-21]. A large number of studies have confirmed that L_{12} phase precipitation strengthening is one of the effective methods to achieve the strength-ductility balance of CoCrFeNi-based HEAs. Yang et al. added a fixed stoichiometric ratio of Ni and Al to the CoCrFeNi HEAs to form a nano-L12 precipitate on the FCC matrix, which effectively improved the strength and maintained good plasticity [22]. He et al. induced the formation of L_{12} coherent nano-γ′ phase in CoCrFeNi HEA by adding a small amount of Al

Received on November 2, 2022; Accepted on December 8, 2022

and Ti, successfully achieving the balance of strength-ductility [23].

For CoCrFeNi HEAs, the corrosion resistance of the alloy can be effectively improved by adding certain alloying elements, which has become one of the important directions of research on the corrosion resistance of HEAs [24-26]. Studies have shown that the composition of the precipitated phase of the alloys and the degree of element segregation directly affect the overall corrosion resistance of the HEA. For example, in the AlxCoCrFeNi alloy, the increasing of the Al content will lead to an increase in the volume fraction of the Cr-depleted body-centered cubic phase, which will reduce the local corrosion resistance [27]. Nevertheless, with the homogenization heat treatment, the degree of element segregation between the precipitated phase and the matrix is reduced, resulting in improving the corrosion resistance of the alloys [28]. Therefore, the composition and compositional regulation of the phase structure play a key role in the corrosion resistance of the alloy. Similar to iron and steel materials, Ni element usually plays the role of austenite stabilization, that is, the higher the content of Ni element, the more stable the FCC structure multi-component solid solution in the HEA. Meanwhile, other phases in the alloys (e.g., BCC structural solid solution phase and B2 phase, σ phase, Laves phase, and other ordered phases) are also gradually suppressed with increasing Ni content [29-30]. In the CoCrFeNi-TiAl HEAs system, the addition of Ti and Al elements will enhance the mechanical properties by forming ordered γ′ strengthening phases, but also consume the group elements in the matrix during the formation of γ′ phases. In particular, the reduction of Ni element in the matrix will lead to a decrease in the stability of the FCC structure matrix, which may lead to a decrease in the corrosion resistance of the matrix, and in turn greatly affect the overall corrosion resistance.

Thus, the main emphasis of this study is to designs and prepares the $CoCrFeNi_xAl_{0.3}Ti_{0.2}$ (x=1.0, 1.25, 1.5, 1.75) HEAs, and to explores the effect of Ni content on the structure, mechanical properties and corrosion resistance of $CoCrFeNi_xAl_{0.15}Ti_{0.1}$ HEAs, as well as to optimize the alloys performance. This work will help to extend the excellent overall performance CoCrFeNi-based HEAs system to provide an important research basis.

2 Material and methods

The $CoCrFeNi_xAl_{0.3}Ti_{0.2}$ HEAs ingots were prepared by melting in vacuum melting furnace using Co, Cr, Fe, Ni, Al, Ti with high-purity (＞ 99.9 wt.%) as raw materials under argon protection. During the smelting process, the samples were re-melted five times at least to ensure the uniformity of the elements. The alloy samples were homogenized at 1200℃ for 18 hours, subsequently by water quenching. All homogenized samples were cold-rolled with a thickness reduction of 60 %, and then aged at 800℃ for 4 h.

The crystal structures of the $CoCrFeNi_xAl_{0.3}Ti_{0.2}$ alloys were examined by X-ray diffractometer (Model D8/Advance, Bruker, Germany) using Cu-Kα radiation with a scanning range of 30 to 90 ° and a step size of 5 °/min. The fracture surfaces of the tensile samples were studied using a scanning electron microscopy (SEM, HITACHI S-4300, Japan). Mechanical tensile tests were performed the dog-bone shaped tensile specimens with 20 × 4 × 2 mm at room temperature by a universal testing machine (CMT4305, New Sansi Laboratory Equipment Co., China) under a strain rate of 5×10^{-4}/s. Electrochemical measurements were carried out using an electrochemical workstation (VersaStat4, Princeton, USA), with a three-electrode system in 3.5 wt.% NaCl solution at room temperature. In three-electrode system, the HEA specimen, platinum electrode and saturated calomel electrode (SCE) were employed as the working, auxiliary and reference electrode, respectively. Before the electrochemical test, all samples were immersed at least 30 minutes until the open circuit potential (OCP) reached a steady state. The potentiodynamic-polarization tests were measured from from an initial potential of -0.25 V (vs. OCP) to the anodic potential with a current density of 2 mA/cm^2 with a scan speed of 1 mV/s. The electrochemical impedance spectroscopy (EIS) was measured at the OCP in the frequency range of 10^5 Hz to 10^{-2} Hz with a potential amplitude of 10 mV.

3 Results

3.1 Microstructure and phase analysis

The XRD patterns of $CoCrFeNi_xAl_{0.15}Ti_{0.1}$ (x=1, 1.25, 1.5, 1.75) HEAs are shown in Figure1. It can be seen that the obvious FCC solid solution structure peaks were identified in all alloys. In general, adding an appropriate amount of Al and Ti to CoCrFeNi alloys is beneficial to the formation of nanoscale L12-γ′ phase, which can be confirmed in TEM experiments in previous work [31].

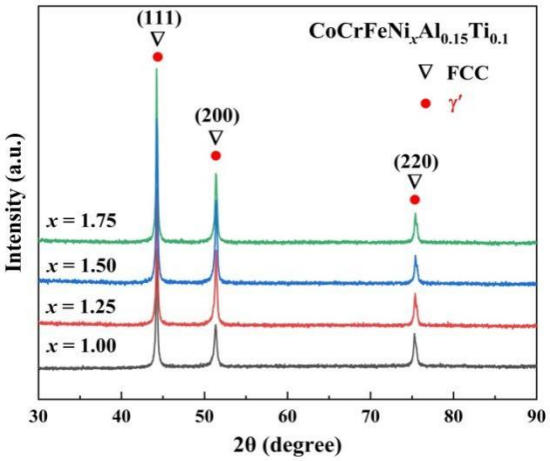

Figure 1 XRD pattern of $CoCrFeNi_xAl_{0.15}Ti_{0.1}$ HEAs

To explore the effect of Ni element content on the phase transition temperature range of HEAs, DSC tests were carried out on $CoCrFeNi_xAl_{0.15}Ti_{0.1}$ alloys with different Ni contents, and the results are shown in Figure 2. As can be seen, with the increase of the Ni content, the

melting point of the HEAs decreases gradually. It should be pointed out that the DSC curves of the four components of the alloys have an obvious exothermic step in the temperature rise stage, indicating that there is an obvious precipitate phase dissolves into the solid-matrix of $CoCrFeNi_xAl_{0.15}Ti_{0.1}$ HEAs during heat treatment temperature. When the Ni content increases from x=1 to x=1.75, the precipitation temperature of ordered γ′ phase in the alloys decreases slowly from 904℃ to 898℃, showing that the addition of Ni element will reduce the thermal stability of the precipitated phase.

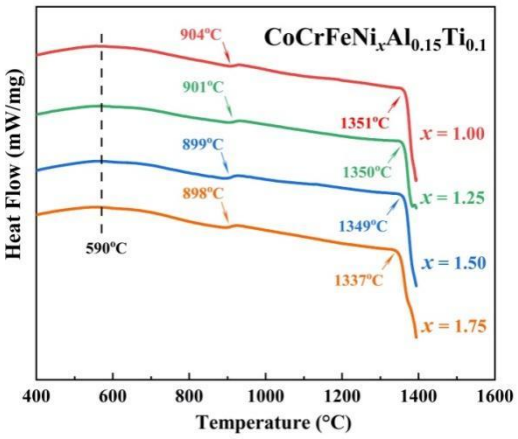

Figure 2 DSC spectrum of $CoCrFeNi_xAl_{0.15}Ti_{0.1}$ (x=1, 1.25, 1.5, 1.75) HEAs

Figure 3 shows the EBSD invert pole figure (IPF) and grain size distribution of $CoCrFeNi_xAl_{0.15}Ti_{0.1}$ HEAs. The HEA grains of the four alloys are basically in an equiaxed state, while the orientation distribution is uniform. Moreover, the grains have no obvious preferred orientation distribution, and there are no large deformed grains. With the increase of Ni content, the average grain size of the alloys decreases first and then increases. The average grain size of $CoCrFeNi_xAl_{0.15}Ti_{0.1}$ HEAs decreased from 14.4μm to 7.6μm when Ni content increased from x=1 to x=1.25. But as the Ni content continues to increase, the average grain size of the x=1.75 alloy begins to increase to 10.7μm. Previous research has shown that the grain size has a direct effect on the strength of the metal, that is, fine grain strengthening [32]. With the gradual refinement of the grains, the number of grain boundaries inside the alloy increases rapidly, resulting in an increase in the hindrance of the grain boundaries to the movement of dislocations during the deformation process, which improves the mechanical properties of the HEAs. Figure4 displays the kernel average misorientation (KAM) maps of $CoCrFeNi_xAl_{0.15}Ti_{0.1}$ HEAs samples. The KAM values generally can be represented as the density of geometrically necessary dislocation (GND) [33]. It can be seen that the dislocations in all alloys are distributed near the grain boundaries. Under the same rolling deformation and heat treatment conditions, the dislocation density in Figure 4(a, c and d) is lower. However, the KAM value in the x=1.25 alloy is significantly higher, indicating that the dislocation density of the alloy accumulated at the grain boundary is greater, which is conducive to improving the initial strain hardening rate of the alloy under small plastic deformation [34].

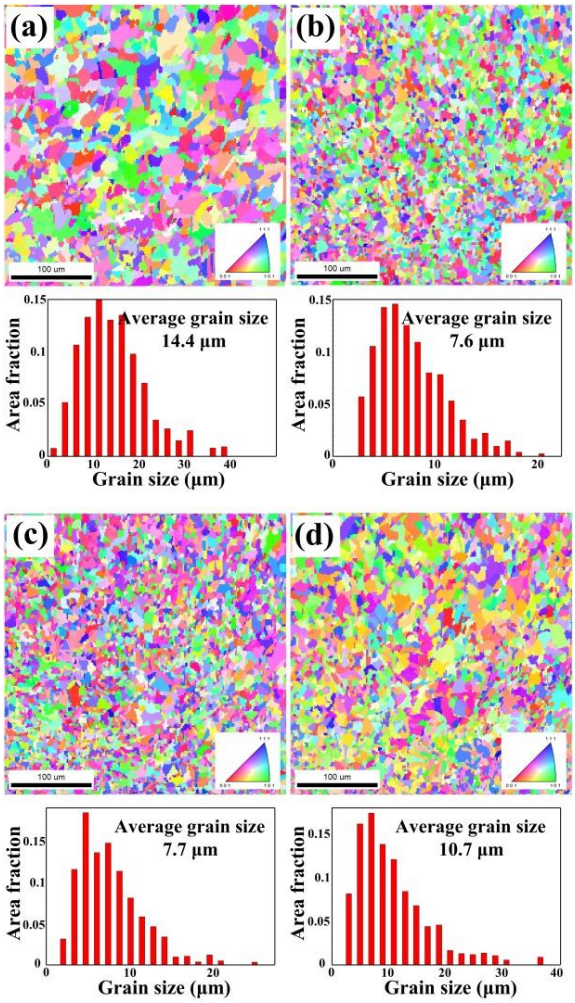

Figure 3 The IPF and grain size distribution of $CoCrFeNi_xAl_{0.15}Ti_{0.1}$ HEAs: (a) x=1, (b) x=1.25, (c) x=1.5, (d) x=1.75

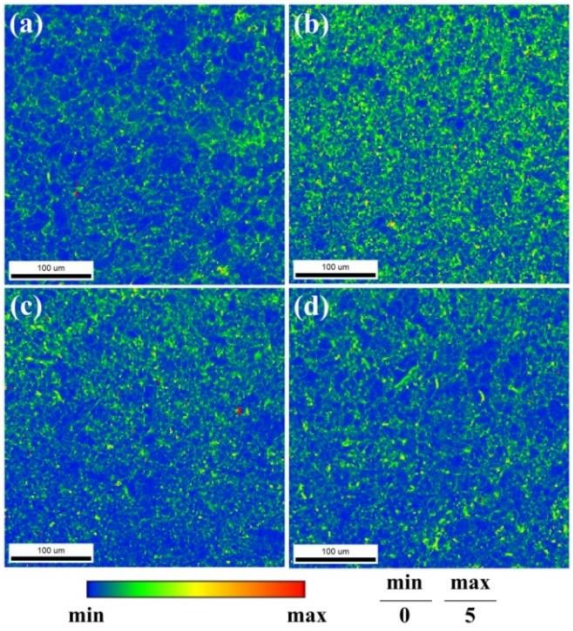

Figure 4 The KAM maps of $CoCrFeNi_xAl_{0.15}Ti_{0.1}$ HEAs: (a) x=1, (b) x=1.25, (c) x=1.5, (d) x=1.75

3.2 Mechanical properties

The tensile engineering stress-strain curves at room temperature of the $CoCrFeNi_xAl_{0.15}Ti_{0.1}$ HEAs are shown in Figure 5(a). Table.1 summarizes the yield strength (σ_{YS}), ultimate tensile strength (σ_{UTS}) and fracture elongation (ε_{FE}) of HEAs. The four components of $CoCrFeNi_xAl_{0.15}Ti_{0.1}$ HEAs exhibiting continuous work hardening behavior until the final plastic instability, while there is no discontinuous yield phenomenon in the transition stage between elastic deformation and plastic deformation. It can be found that as the Ni content increased to x=1.25, the comprehensive mechanical properties of the $CoCrFeNi_{1.25}Al_{0.15}Ti_{0.1}$ HEAs reached the optimum, and the yield strength, ultimate tensile strength and fracture elongation were 800.4 MPa, 1172 MPa and 27.1%, respectively. After the end of the elastic stage, $CoCrFeNi_{1.25}Al_{0.15}Ti_{0.1}$ HEAs exhibits a short yield plateau and begins to show significant work-hardening behavior after the end of the yield stage. As the Ni content continues to increase, the mechanical properties of the $CoCrFeNi_xAl_{0.15}Ti_{0.1}$ HEAs begin to decline, and the plastic deformation ability also decreases. Figure 5 (b) shows the work-hardening behavior of $CoCrFeNi_xAl_{0.15}Ti_{0.1}$ HEAs. All alloys exhibit a typical multi-stage work-hardening rate curve. The first stage is the transition from elastic to plastic deformation. Due to the low density of mobile dislocations at the onset of plastic deformation, the work hardening rate rapidly decreases to a negative value, which corresponds to the yield drop in the engineering stress-strain curve. The second stage of work hardening increases significantly, which may be related to the twinning related deformation mechanisms generated during deformation [4,35]. The anomalous increase in strain hardening rate in this stage is crucial for maintaining the plastic stability of the alloy [36]. The third stage of work-hardening rate decreases slowly and corresponds to the longer plastic deformation phase of the engineering stress-strain curve. In this stage, the work-hardening rate gradually decreases until a local stress concentration occurs, leading to catastrophic fracture.

Table 1 The yield strength, ultimate tensile strength and fracture elongation of $CoCrFeNi_xAl_{0.15}Ti_{0.1}$ HEAs

Alloys	σ_{YS} (MPa)	σ_{UTS} (MPa)	ε_{FE} (%)
$CoCrFeNiAl_{0.15}Ti_{0.1}$	739.8	1142.6	29.1
$CoCrFeNi_{1.25}Al_{0.15}Ti_{0.1}$	800.4	1172.9	27.1
$CoCrFeNi_{1.5}Al_{0.15}Ti_{0.1}$	778.9	1156.2	24.9
$CoCrFeNi_{1.75}Al_{0.15}Ti_{0.1}$	745.0	1121.3	24.5

Figure 6 is the SEM image of the tensile sample fracture of $CoCrFeNi_xAl_{0.15}Ti_{0.1}$ HEAs. A large number of dimples and a small number of cleavage fracture planes can be found in the tensile sections of all samples, meaning that the tensile fracture modes of the four groups of samples are dominated by ductile fracture and shear fracture. In general, the size of fracture dimples is related to the size of grains, because grain boundaries are the starting point of pores. The finer the grain, the smaller the dimple size [37]. In addition, the separation of the precipitated phase and the matrix during deformation and the fragmentation of the precipitated phase can also lead to the formation of pores [38]. Thus, the dimples at the fracture of the samples with Ni content of x=1.25 and x=1.5 are smaller, while the number of cleavage fracture planes is also increase. This may be related to the promotion of the precipitation of γ' phase after a small increase in Ni content. On the one hand, the formation of precipitated phases causes the strengthening effect of the second phase. On the other hand, the precipitated phases can also play a role in refining grains [39]. When the Ni content continued to increase to x=1.75, the dimple depth at the fracture site of the sample began to become shallower, and the cleavage area began to increase, indicating a decrease in the ductile fracture of the sample.

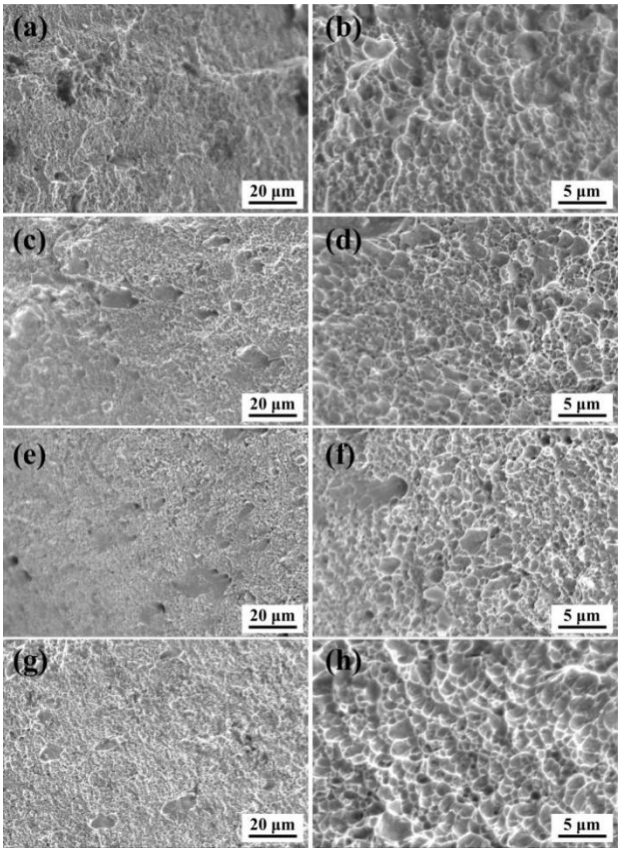

Figure 6 Fracture morphology and high-magnification fracture morphology of tensile samples of $CoCrFeNi_xAl_{0.15}Ti_{0.1}$ HEA: (a, b) x=1, (c, d) x=1.25, (e, f) x=1.5, (g, h) x=1.75

3.3 Corrosion resistance

Figure 7 illustrates the potential polarization curves of the $CoCrFeNi_xAl_{0.15}Ti_{0.1}$ HEAs under 3.5 wt.% NaCl solution at room temperature. The results of the electrochemical corrosion parameters (corrosion potential Ecorr, corrosion current icorr) are listed in Table 2. It can be found that the polarization curves of $CoCrFeNi_xAl_{0.15}Ti_{0.1}$ HEAs are similar, showing the same active-to-passive corrosion behavior. Based on electrochemical theory, the lower the corrosion current of a material, the better its corrosion resistance. Thus, all

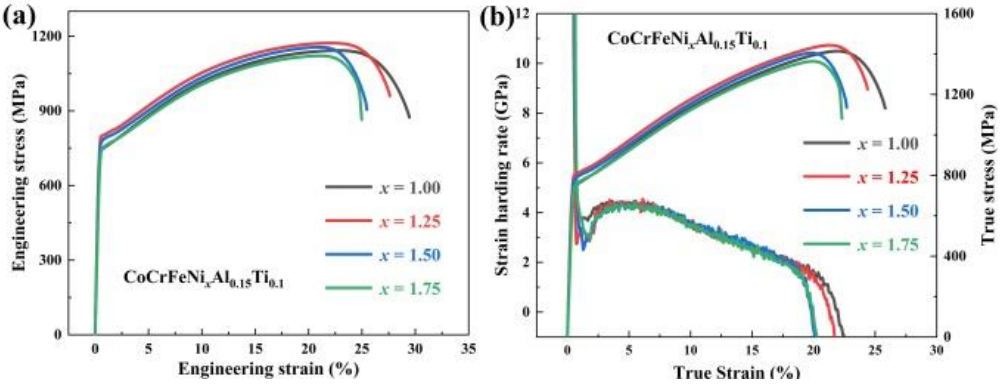

Figure 5 The mechanical properties of $CoCrFeNi_xAl_{0.15}Ti_{0.1}$ (x=1, 1.25, 1.5, 1.75) HEAs at room temperature (a) engineering stress-strain, (b) true stress-strain curve and work hardening rate

$CoCrFeNiAl_{0.15}Ti_{0.1}$ HEAs demonstrate better corrosion resistance. Additionally, the dislocations also play a great influence on the corrosion resistance of alloys, which will promote the passive film on the surface of the alloys and the diffusion of cation vacancies within the matrix [40]. These point defects in the environment of chlorine-containing corrosive solutions will accelerate the destruction of the surface passive film, reducing the corrosion resistance of the alloys. With the increase of Ni element in the alloys to x=1.25, the corrosion current density of the alloys reaches 9.19×10^{-8}A/cm^2, indicating that the corrosion resistance of x=1.25 alloy are the worst at the corrosion potential. However, the corrosion current density of the all alloys still maintains the same order of magnitude, implying that the HEA of this system possess good corrosion resistance.

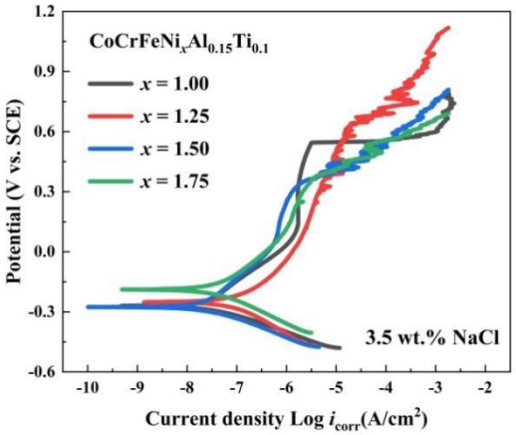

Figure 7 Potentiodynamic polarization curves of $CoCrFeNi_xAl_{0.15}Ti_{0.1}$ HEAs

In the corrosion resistance of materials, the pitting potential (Epit) is an important performance index parameter that characterizes the material's pitting resistance. Although the corrosion current density of $CoCrFeNi_{1.25}Al_{0.15}Ti_{0.1}$ HEAs is the highest, the breakdown potential reaches 0.639 V (vs. SCE), indicating that the formation of passive film of this component is more stable at high potentials. With the further increase of Ni element, the pitting corrosion potential of the material gradually decreases. Previous studies have shown that Cr element is a key element of stainless steel. In seawater, Cr element can form a dense Cr_2O_3 film on the surface of stainless steel, which greatly improves the resistance of the material to the erosion of chloride ions [41]. For $CoCrFeNi_xAl_{0.15}Ti_{0.1}$ HEAs, when the content of Ni in the alloy is excessive, the reduction of pitting corrosion resistance in the alloys may be related to the reduction of the relative content of Cr in the alloys.

Table 2 Corrosion kinetic parameters of $CoCrFeNi_xAl_{0.15}Ti_{0.1}$ HEAs

Alloys	Ecorr (V_{SCE})	Icorr (A/cm^2)	Epit (V_{SCE})
$CoCrFeNiAl_{0.15}Ti_{0.1}$	-0.265	2.86×10^{-8}	0.544
$CoCrFeNi_{1.25}Al_{0.15}Ti_{0.1}$	-0.256	9.19×10^{-8}	0.639
$CoCrFeNi_{1.5}Al_{0.15}Ti_{0.1}$	-0.268	3.23×10^{-8}	0.356
$CoCrFeNi_{1.75}Al_{0.15}Ti_{0.1}$	-0.187	3.89×10^{-8}	0.379

In order to further understand the corrosion mechanism of $CoCrFeNi_{1.25}Al_{0.15}Ti_{0.1}$ HEAs under the open circuit potential, the material was analyzed by EIS test. Figure 8 shows the Nyquist plot and Bode plot results of $CoCrFeNixAl_{0.15}Ti_{0.1}$ HEAs. All response results present a single capacitive semicircle, indicating a passive film with the same structure. For the Nyquist plot, the larger the diameter of the arc, the more stable the passive film formed on the surface of the alloys [42]. In Figure 8 (a), the corrosion resistance trend of $CoCrFeNi_xAl_{0.15}Ti_{0.1}$ HEAs is basically consistent with the potentiodynamic polarization curve. In addition, Figure 8 (b) shows the Bode plots of different alloys, and the phase angles of all alloys tend to be -80 ° in a wide frequency range, meaning a stable passive film is formed on the surface of the alloys.

According to the semicircular arc characteristics of the Nyquist plot and the corrosion characteristics of the alloys, Figure 8 (a) shows the equivalent circuit applicable to the alloy system. In this circuit, Rs and Rt represent the resistance of the solution and the passive film, respectively [43]. Based on this fitting circuit simulation, the electrochemical impedance fitting parameters of the $CoCrFeNi_xAl_{0.15}Ti_{0.1}$ HEAs are listed in Table.3. Generally, the higher the resistance Rt of the passive film, the better the protective effect of the passive film. Thus, $CoCrFeNiAl_{0.15}Ti_{0.1}$ HEAs display

better passive film stability at open circuit potential.

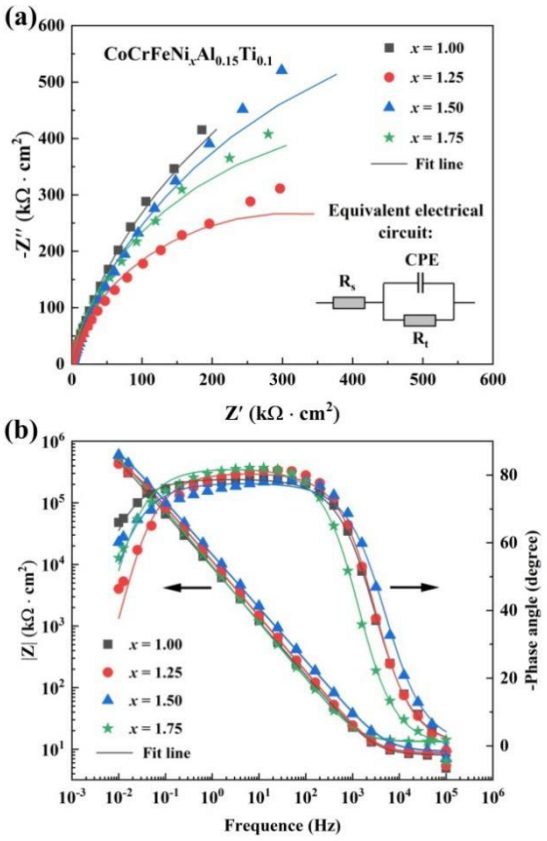

Figure 8 EIS response of $CoCrFeNi_xAl_{0.15}Ti_{0.1}$ HEAs: (a) Nyquist plot and equivalent circuit, (b) Bode plot

Table 3 Impedance fitting parameters of $CoCrFeNixAl_{0.15}Ti_{0.1}$ by the equivalent circuit.

Alloys	Rs /Ω*cm^2	Y (CPE) /(F*cm^{-2})	n	Rt /Ω*cm^2
$CoCrFeNiAl_{0.15}Ti_{0.1}$	7.99	2.23×10^{-5}	0.88	1.73×10^{6}
$CoCrFeNi_{1.25}Al_{0.15}Ti_{0.1}$	8.60	1.70×10^{-5}	0.90	6.30×10^{5}
$CoCrFeNi_{1.5}Al_{0.15}Ti_{0.1}$	9.18	1.41×10^{-5}	0.86	1.53×10^{6}
$CoCrFeNi_{1.75}Al_{0.15}Ti_{0.1}$	13.26	2.00×10^{-5}	0.91	9.70×10^{5}

4 Conclusions

In this work, the effects of Ni on the microstructure, mechanical properties and corrosion resistance of $CoCrFeNi_xAl_{0.15}Ti_{0.1}$ HEAs have been systematically investigated, and the main conclusions are as follows:

$CoCrFeNi_xAl_{0.15}Ti_{0.1}$ HEAs consists of a typical dual-phase structure of FCC + γ′ phases. The crystals in the all alloys exhibit equiaxed crystal morphology, and the $CoCrFeNi_{1.25}Al_{0.15}Ti_{0.1}$ alloy has the smallest grain size, with an average grain size of 7.6 μm.

The yield strength and tensile strength of $CoCrFeNi_xAl_{0.15}Ti_{0.1}$ HEAs increased first and then decreased with the increase of Ni content, but the tensile plasticity remained at a high level. Especially, the yield strength and tensile strength of $CoCrFeNi_{1.25}Al_{0.15}Ti_{0.1}$ alloy reached 800 MPa and 27.1%, respectively.

Due to the formation of a stable passive film on the surface, $CoCrFeNi_xAl_{0.15}Ti_{0.1}$ HEAs display good corrosion resistance under corrosion potential. Excessive Ni element in the alloy will reduce the pitting corrosion resistance of the alloy.

Acknowledgements

This work is supported by the National Key R&D Program of China (Grant No. 2020YFA0405700), the Inner Mongolia Science and Technology Major Project (No. 2020ZD0011).

References

[1] E.P. George, D. Raabe, R.O. Ritchie, High-entropy alloys, Nature Reviews Materials [J].2029, 4(8): 515-534.

[2] Q. Ding, Y. Zhang, X. Chen, et al.. Tuning element distribution, structure and properties by composition in high-entropy alloys, Nature [J].2019, 574(7777): 223-227.

[3] C.M. Lin, H.L. Tsai, H.Y. Bor. Effect of aging treatment on microstructure and properties of high-entropy Cu0.5CoCrFeNi alloy, Intermetallics [J].2010,18(6): 1244-1250.

[4] G. Laplanche, A. Kostka, O.M. Horst, et al.. Microstructure evolution and critical stress for twinning in the CrMnFeCoNi high-entropy alloy, Acta Mater [J]. 2016(118): 152-163.

[5] X. Yang, Y. Zhang. Prediction of high-entropy stabilized solid-solution in multi-component alloys, Mater. Chem. Phys. 2012,132(2): 233-238.

[6] Z.G. Wang, W. Zhou, L.M. Fu, et al.. Effect of coherent L12 nanoprecipitates on the tensile behavior of a fcc-based high-entropy alloy, Mater. Sci. Eng. 2017(696): 503-510.

[7] W. Wang, W. Qi, L. Xie, X. Yang, J. Li, Y. Zhang, Microstructure and Corrosion Behavior of (CoCrFeNi)95Nb5 High-Entropy Alloy Coating Fabricated by Plasma Spraying, Materials. 2019,12(5): 694.

[8] W. Qi, W. Wang, X. Yang, et al.. Effect of Zr on phase separation, mechanical and corrosion behavior of heterogeneous CoCrFeNiZrx high-entropy alloy, J Mater Sci Technol. 2022(109): 76-85.

[9] W. Huo, F. Fang, H. Zhou, et al.. Remarkable strength of CoCrFeNi high-entropy alloy wires at cryogenic and elevated temperatures, Scripta Mater. 2017(141): 125-128.

[10] P. Wu, K. Gan, D. Yan, et al.. A non-equiatomic FeNiCoCr high-entropy alloy with excellent anti-corrosion performance and strength-ductility synergy, Corros. Sci. 2021(183): 13.

[11] H. C. Liu, C. W. Tsai. Effect of Ge addition on the microstructure, mechanical properties, and corrosion behavior of CoCrFeNi high-entropy alloys, Intermetallics. 2021(132):47.

[12] Y. Fu, J. Li, H. Luo, et al.. Recent advances on environmental corrosion behavior and mechanism of high-entropy alloys, J Mater Sci Technol. 2021(80): 217-233.

[13] E. Nembach, G. Neite. Precipitation hardening of superalloys by ordered γ′-particles, Prog. Mater Sci. 1985,29(3): 177-319.

[14] W. F. Miao, D. E. Laughlin. Precipitation hardening in aluminum alloy 6022, Scripta Mater. 1999,40(7): 873-878.

[15] M. J. Yao, E. Welsch, D. Ponge, et al.. Strengthening and strain hardening mechanisms in a precipitation-hardened high-Mn lightweight steel, Acta Mater. 2017(140):258-273.
[16] D. Chen, F. He, B. Han, et al.. Synergistic effect of Ti and Al on L12-phase design in CoCrFeNi-based high entropy alloys, Intermetallics. 2019(110):67-68.
[17] W.H. Liu, T. Yang, C.T. Liu. Precipitation hardening in CoCrFeNi-based high entropy alloys, Mater. Chem. Phys. 2018(210):2-11.
[18] Y. Yu, F. He, Z. Qiao, et al.. Effects of temperature and microstructure on the triblogical properties of CoCrFeNiNbx eutectic high entropy alloys, J. Alloys Compd. 2019(775): 1376-1385.
[19] W. Liu, J. He, H. Huang, et al.. Effects of Nb additions on the microstructure and mechanical property of CoCrFeNi high-entropy alloys, Intermetallics. 2015(60): 1-8.
[20] H. Ma, C.H. Shek, Effects of Hf on the microstructure and mechanical properties of CoCrFeNi high entropy alloy, J. Alloys Compd. 2020(827):456.
[21] H. Jiang, K. Han, D. Qiao, et al.. Effects of Ta addition on the microstructures and mechanical properties of CoCrFeNi high entropy alloy, Mater. Chem. Phys. 2018(210): 43-48.
[22] F. Zheng, G. Zhang, X. Chen, et al.. A new strategy of tailoring strength and ductility of CoCrFeNi based high-entropy alloy, Mater. Sci. Eng. 2020(774):98-102.
[23] J.Y. He, H. Wang, H.L. Huang, et al.. A precipitation-hardened high-entropy alloy with outstanding tensile properties, Acta Mater. 2016(102): 187-196.
[24] W. Wang, J. Wang, Z. Sun, et al.. Effect of Mo and aging temperature on corrosion behavior of (CoCrFeNi)100-xMox high-entropy alloys, J. Alloys Compd. 2020(812):152139.
[25] Y. J. Hsu, W. C. Chiang, J. K. Wu, Corrosion behavior of FeCoNiCrCux high-entropy alloys in 3.5% sodium chloride solution, Mater. Chem. Phys. 2005,92(1): 112-117.
[26] P. Muangtong, A. Rodchanarowan, D. Chaysuwan, et al.. The corrosion behaviour of CoCrFeNi-x (x=Cu, Al, Sn) high entropy alloy systems in chloride solution, Corros. Sci. 2020(172):1-2.
[27] Y. Shi, B. Yang, X. Xie, et al.. Corrosion of AlxCoCrFeNi high-entropy alloys: Al-content and potential scan-rate dependent pitting behavior, Corros. Sci. 2017(119): 33-45.
[28] Y. Shi, L. Collins, R. Feng, et al.. Homogenization of AlxCoCrFeNi high-entropy alloys with improved corrosion resistance, Corros. Sci. 2018(133):120-131.
[29] C. Liu, W. Peng, C.S. Jiang, et al.. Composition and phase structure dependence of mechanical and magnetic properties for AlCoCuFeNix high entropy alloys, J Mater Sci Technol. 2019,35(6):1175-1183.
[30] C. C. Juan, C. Y. Hsu, C. W. Tsai, et al.. On microstructure and mechanical performance of AlCoCrFeMo0.5Nix high-entropy alloys, Intermetallics. 2013,32(0):401-407.
[31] W. Qi, W. Wang, X. Yang, et al.. Effects of Al and Ti co-doping on the strength-ductility- corrosion resistance of CoCrFeNi-AlTi high-entropy alloys, J. Alloys Compd. 2022(925):166751.
[32] S. Gangireddy, B. Gwalani, R.S. Mishra. Grain size dependence of strain rate sensitivity in a single phase FCC high entropy alloy Al0.3CoCrFeNi, Mater. Sci. Eng. 2018(736): 344-348.
[33] J. Su, D. Raabe, Z. Li. Hierarchical microstructure design to tune the mechanical behavior of an interstitial TRIP-TWIP high-entropy alloy, Acta Mater. 2019(163): 40-54.
[34] N.K. Adomako, G. Shin, N. Park, et al.. Laser dissimilar welding of CoCrFeMnNi-high entropy alloy and duplex stainless steel, J Mater Sci Technol. 2021(85): 95-105.
[35] W.H. Liu, Z.P. Lu, J.Y. He, et al.. Ductile CoCrFeNiMox high entropy alloys strengthened by hard intermetallic phases, Acta Mater. 2016(116): 332-342.
[36] T. Yang, Y.L. Zhao, J.H. Luan, et al.. Nanoparticles-strengthened high-entropy alloys for cryogenic applications showing an exceptional strength-ductility synergy, Scripta Mater. 2019(164):30-35.
[37] M. H. Cai, C. Y. Lee, Y. K. Lee. Effect of grain size on tensile properties of fine-grained metastable β titanium alloys fabricated by stress-induced martensite and its reverse transformations, Scripta Mater. 2012,66(8): 606-609.
[38] O. León-García, R. Petrov, L.A.I. Kestens. Void initiation at TiN precipitates in IF steels during tensile deformation, Mater. Sci. Eng. 2010,527(16-17): 4202-4209.
[39] J. He, N. Li, S.K. Makineni, et al.. Effects of minor Nb alloying on the thermal stability and mechanical responses of a γ/γ′ type high-entropy alloy with high Fe content, Mater. Sci. Eng. 2022(851):6-8.
[40] Y. Wang, J. Jin, M. Zhang, et al.. Influence of plastic deformation on the corrosion behavior of CrCoFeMnNi high entropy alloy, J. Alloys Compd. 2022(891):79-92.
[41] J. B. Lee. Effects of alloying elements, Cr, Mo and N on repassivation characteristics of stainless steels using the abrading electrode technique, Mater. Chem. Phys. 2006,99(3): 224-234.
[42] Z. Xu, H. Zhang, X. Du, et al.. Corrosion resistance enhancement of CoCrFeMnNi high-entropy alloy fabricated by additive manufacturing, Corros. Sci. 2020(177):34-36.
[43] H. Luo, Z. Li, A.M. Mingers, et al.. Corrosion behavior of an equiatomic CoCrFeMnNi high-entropy alloy compared with 304 stainless steel in sulfuric acid solution, Corros. Sci. 2018(134): 131-139.

Publisher: Viser Technology Pte. Ltd.

URL: www.viserdata.com

Add.:21 Woodlands Close, #08-18,

Primz Bizhub SINGAPORE (737854)